0830-L-02

NAS 1.29/3-2:98-08

NASA Tech Briefs

National Aeronautics and
Space Administration

Electronic Components and Circuits

Electronic Systems

Physical Sciences

Materials

Computer Programs

Mechanics

Machinery

Fabrication Technology

Mathematics and Information Sciences

Life Sciences

98-08

August 1998

COMPLETED

NE 98-034702

INTRODUCTION

Tech Briefs are short announcements of new technology derived from the research and development activities of the National Aeronautics and Space Administration. These Briefs emphasize information considered likely to be transferable across industrial, regional, or disciplinary lines and are issued to encourage commercial application.

Availability of NASA Tech Briefs and TSP's

Distribution of NASA Tech Briefs, a monthly periodical publication, is limited to engineers in U.S. Industry and to other domestic technology transfer agents. Requests for individual Tech Briefs or for Technical Support Packages (TSP's) announced herein should be addressed to

NASA Center for AeroSpace Information
Technology Transfer Office
800 Elkridge Landing Rd.
Linthicum Heights, MD 21090-2934
Telephone No. (301) 621-0245

Please reference the three-letter, five-digit control number located at the end of each Tech Brief. Information on NASA's Technology Utilization Program, its documents, and services is also available at the same facility.

Technology Utilization Officers and Patent Counsels are located at NASA field installations to provide technology-transfer access to industrial users. Inquiries can be made by writing to NASA field installations listed below.

Technology Utilization Officers and Patent Counsels

Ames Research Center
Technology Utilization Officer
Mail Code 223-3
Moffett Field, CA 94035

Patent Counsel
Mail Code 200-11
Moffett Field, CA 94035

Goddard Space Flight Center
Technology Utilization Officer
Mail Code 702-1
Greenbelt, MD 20771

Patent Counsel
Mail Code 204
Greenbelt, MD 20771

Lyndon B. Johnson Space Center
Technology Utilization Officer
Mail Code IC 4
Houston, TX 77058

Patent Counsel
Mail Code AL3
Houston, TX 77058

John F. Kennedy Space Center
Technology Utilization Officer
Mail Stop PT-PMO-A
Kennedy Space Center, FL 32899

Patent Counsel
Mail Code PT-PAT
Kennedy Space Center, FL 32899

Langley Research Center
Technology Utilization Officer
Mail Stop 143
Hampton, VA 23665

Patent Counsel
Mail Code 279
Hampton, VA 23665

Lewis Research Center
Technology Utilization Officer
Mail Stop 7-3
21000 Brookpark Road
Cleveland, OH 44135

Patent Counsel
Mail Code LE-LAW
21000 Brookpark Road
Cleveland, OH 44135

Jet Propulsion Laboratory
Technology Utilization Officer
Mail Stop 156-211
4800 Oak Grove Drive
Pasadena, CA 91109

NASA Resident Office-JPL
Technology Utilization Officer
Mail Stop 180-801
4800 Oak Grove Drive
Pasadena, CA 91109

Patent Counsel
Mail Code 180-801
4800 Oak Grove Drive
Pasadena, CA 91109

George C. Marshall Space Flight Center
Technology Utilization Officer
Code AT01
Marshall Space Flight Center, AL 35812

Patent Counsel
Mail Code CC01
Marshall Space Flight Center, AL 35812

John C. Stennis Space Center
Technology Utilization Officer
Code HA-30
Stennis Space Center, MS 39529

NASA Headquarters
Technology Utilization Officer
Code CU
Washington, DC 20546

Assistant General Counsel for Patent Matters
Code GP
Washington, DC 20546

Dryden Flight Research Center
Technology Utilization Officer
M/S D21-31
Bldg. 4832 Whse 7
Lilly Dr.
Edwards, CA 93523

BLANK PAGE

NASA TechBriefs

National Aeronautics and
Space Administration

August 1998
98-08

5 Electronic Components and Circuits

13 Electronic Systems

19 Physical Sciences

29 Materials

37 Computer Programs

41 Mechanics

45 Machinery

This document was prepared under the sponsorship of the National Aeronautics and Space Administration. Neither the United States Government nor any person acting on behalf of the United States Government assumes any liability resulting from the use of the information contained in this document, or warrants that such use will be free from privately owned rights.

BLANK PAGE

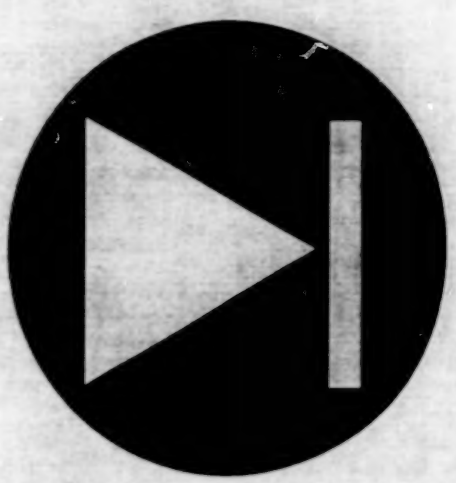

Electronic Components and Circuits

Hardware, Techniques, and Processes

7 TRL Fixture for Cryogenic Testing of Microwave Components
8 Stable Breakdown Obtained in Silicon Carbide Rectifiers
9 Photochromic Image-Plane Filter Extends Dynamic Range of CCD
10 Self-Checking Circuitry for Detecting Single-Event Latchups

BLANK PAGE

TRL Fixture for Cryogenic Testing of Microwave Components

One can complete a test without interrupting a cryogenic and/or vacuum condition.

Lewis Research Center, Cleveland, Ohio

A single-block fixture enables the rapid and accurate electrical characterization of planar microwave electronic components, by use of the through-reflect-line (TRL) technique, in air or in a vacuum at any temperature from ambient down to cryogenic temperatures. Heretofore, the TRL technique has involved the use of a split-block fixture in a procedure that unavoidably and undesirably includes breaking vacuum and/or thermal cycling back to room temperature. The design of the present single-block fixture makes it possible to complete the testing of a microwave component without interrupting a vacuum and/or cryogenic condition.

A planar microwave device under test (DUT) is typically characterized by use of an automatic network analyzer (ANA). To be able to characterize the DUT as a discrete, isolated device, one must be able to compensate mathematically for the electromagnetic characteristics of the test fixture, coaxial-to-microstrip transitions, coaxial cables, and other components used to couple test signals between the ANA and the DUT. For this purpose, one must perform calibration measurements to characterize the ensemble of all components of the test system up to a set of reference planes where the DUT is to be installed in the test fixture.

For calibration measurements, one inserts a calibration standard — a device with known electromagnetic characteristics — in place of the DUT. In the split-block version of the TRL technique, the split block is configured in three different ways to obtain different calibration standards (see Figure 1). The split-block version of the TRL technique works well at room temperature. However, this version is too cumbersome for vacuum and cryogenic testing, in that the block must be rewired and reconfigured between calibration steps. The rewiring and reconfiguration must be performed under ambient conditions and they take time, adding to the cost of testing. During the rewiring and reconfiguration time, ANA reference levels can drift, with consequent increases in measurement errors. In contrast, there is no need to reconfigure or rewire the present single-block fixture; therefore, calibration can be completed more easily and quickly at any temperature, and measurements can be more repeatable.

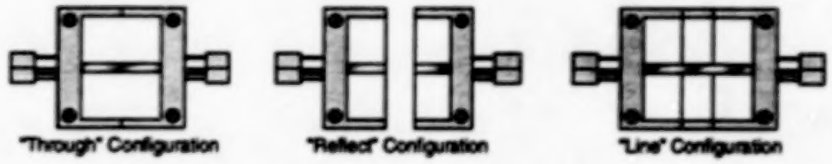

Figure 1. The Predecessor to the Single-Block Fixture is a split-block fixture that is used in three different configurations.

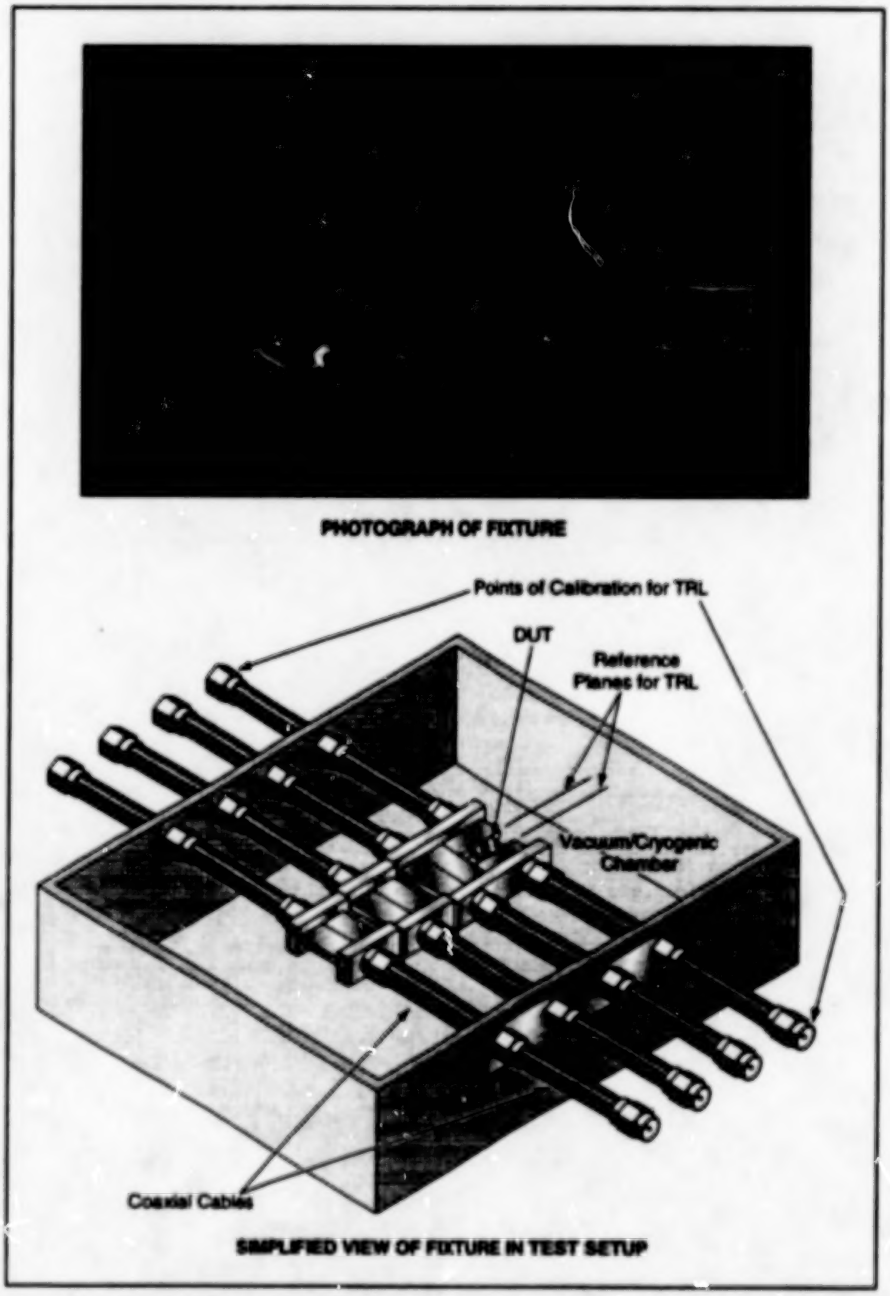

Figure 2. The Single-Block TRL Fixture holds the DUT and the calibration standards in the vacuum/cryogenic chamber. Connections between and external ANA and one of the devices on the fixture are made through the appropriate input/output pair of coaxial cables.

The single-block fixture (see Figure 2) holds the DUT plus through, reflect, and delay (line) calibration standards in their prescribed test setups and is placed in a vacuum/cryogenic chamber. The fixture includes a 0.010-in. (254-μm)-thick alumina substrate with etched gold strips serving as transmission-line conductors. The input and output transmission lines are patterned for a characteristic impedance of 50 Ω.

Connections between external circuitry and these input/output lines are made via coaxial connectors and coaxial-to-microstrip transitions. Coaxial cables run from these connectors to points outside the vacuum/cryogenic chamber. There are no moving parts and there is no switching of electrical connections in the vacuum/cryogenic chamber. Instead, access to the DUT or to one of the calibration standards is gained by connecting, outside the vacuum/cryogenic chamber, to the appropriate coaxial cable.

This work was done by F. A. Miranda and B. T. Ebihara of **Lewis Research Center** *and A. S. Creason of Ohio Northern University, M. Mejia of University of Pennsylvania, and S. S. Toncich of Bird Electronics. Further information is contained in a TSP [see page 1].*

Inquiries concerning rights for the commercial use of this invention should be addressed to NASA Lewis Research Center, Commercial Technology Office, Attn: Tech Brief Patent Status, Mail Stop 7–3, 21000 Brookpark Road, Cleveland, Ohio 44135. Refer to LEW-16567.

Stable Breakdown Obtained in Silicon Carbide Rectifiers

Damaging junction hot spots and current concentrations can be eliminated.

Lewis Research Center, Cleveland, Ohio

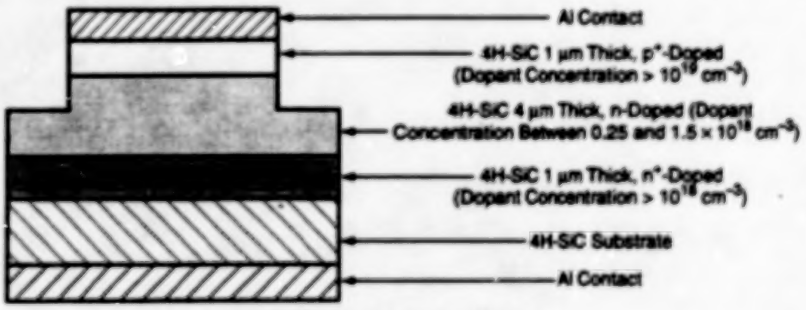
Al Contact
4H-SiC 1 μm Thick, p⁺-Doped (Dopant Concentration > 10¹⁹ cm⁻³)
4H-SiC 4 μm Thick, n-Doped (Dopant Concentration Between 0.25 and 1.5 × 10¹⁸ cm⁻³)
4H-SiC 1 μm Thick, n⁺-Doped (Dopant Concentration > 10¹⁸ cm⁻³)
4H-SiC Substrate
Al Contact

CROSS SECTION OF DIODE

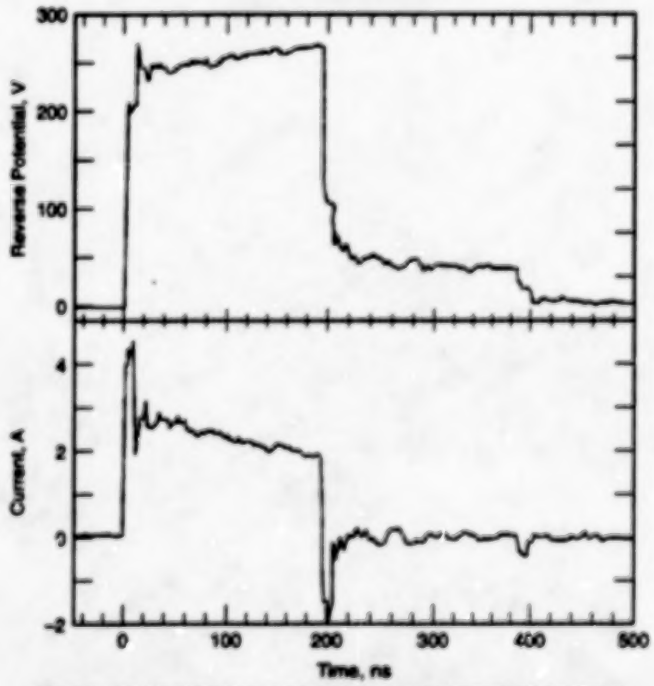

RESPONSE OF DIODE TO A REVERSE-BIAS OVERVOLTAGE PULE

The Voltage and Current Responses of the Diode are consistent with a positive temperature coefficient of breakdown voltage. Ignoring the displacement-current spike at the leading edge of the current waveform, the peak breakdown current of about 2.5 A corresponds to a current density of about 5×10^4 A/cm².

Experiments have revealed that stable breakdown-voltage characteristics can be achieved in silicon carbide rectifiers. Stable breakdown-voltage characteristics are essential to the ability to withstand overvoltage transients and are therefore necessary for reliability in high-power semiconductor switching and rectifying devices.

Silicon carbide semiconductor devices can function under high-temperature, high-power, and high-ionizing-radiation conditions beyond the endurance limits of silicon semiconductor devices. Consequently, SiC devices are undergoing development for eventual use in potential applications that include high-voltage switching in electric-power distribution and electric vehicles, increasingly powerful microwave electronic circuits for radar and cellular communications, and sensors and controls for advanced, cleaner-burning, more-efficient engines. However, prior to the experiments reported here, SiC semiconductor devices had exhibited unstable breakdown-voltage characteristics and were therefore questionable for incorporation into high-power circuits.

In this context, a stable or unstable breakdown-voltage characteristic of a semiconductor rectifier is synonymous with a positive or negative value, respectively, of the temperature coefficient of breakdown voltage. Silicon power rectifiers in use today are highly reliable, partly because they have positive temperature coefficients of breakdown voltages.

During large overvoltage transients, a device can become momentarily reverse-biased at a potential greater than its reverse breakdown voltage. If the device has a negative temperature coefficient of

breakdown voltage, then local junction heating from breakdown current causes the local breakdown voltage to decrease, thereby giving rise to a further local increase in breakdown current. The breakdown current becomes concentrated into one or more high-current-density filaments at junction hot spots, which leads to physical junction damage and device failure. If the device has a positive temperature coefficient of breakdown voltage, then local junction heating from breakdown current increases the local breakdown voltage, preventing local concentration of breakdown current; thus, breakdown current distributes nearly evenly across the entire area of the diode junction.

The experiments were performed to determine whether the unstable breakdown observed previously is a fundamental property of SiC or whether it arises because of impurities and crystalline imperfections that could be reduced by improvements in techniques for growing SiC crystals. For the experiments, SiC rectifier diodes were fabricated by use of the crystal-growth process described in "Chemical Vapor Deposition of Silicon Carbide With Controlled Doping" (LEW-15803), *NASA Tech Briefs*, Vol. 20, No. 12 (December 1996), page 80. The figure shows the diode structure and current and voltage waveforms recorded when one of these diodes was subjected to an overvoltage pulse with a duration of 200 ns. These waveforms show that as the device becomes heated by the breakdown current during the pulse interval, the voltage across the device increases, while the current through the device decreases; this behavior is consistent with a positive temperature coefficient of breakdown voltage and thus with a stable breakdown-voltage characteristic needed for reliability. The diode sustained repeated overvoltage pulses without measurable degradation of its junction.

This work was done by Philip G. Neudeck of **Lewis Research Center** *and Chris Fazi of U.S. Army Research Laboratory. Further information is contained in a TSP [see page 1].*

Inquiries concerning rights for the commercial use of this invention should be addressed to NASA Lewis Research Center, Commercial Technology Office, Attn: Tech Brief Patent Status, Mail Stop 7–3, 21000 Brookpark Road, Cleveland, Ohio 44135. Refer to LEW-16551.

Photochromic Image-Plane Filter Extends Dynamic Range of CCD

The material of self-adjusting sunglasses enables CCD imaging of high-contrast scenes.

NASA's Jet Propulsion Laboratory, Pasadena, California

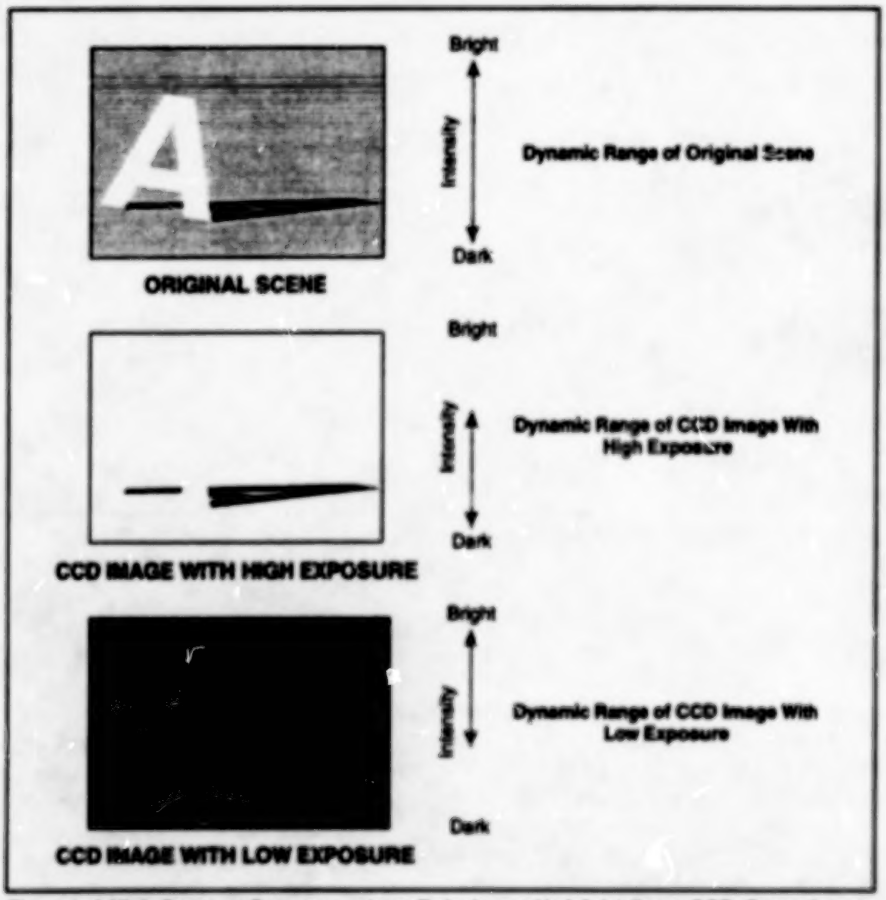

Figure 1. A High-Contrast Scene cannot readily be imaged in full detail on a CCD. Depending on the optical and electronic camera settings, the image tends to be either overexposed in the bright areas or underexposed in the dark areas.

A simple technique for extending the dynamic range of a charge-coupled-device (CCD) video camera involves the use of photochromic material — the same material used in self-adjusting sunglasses. The dynamic range of an image is the ratio between the maximum and minimum brightness levels in the image. The dynamic range of a CCD is the ratio between an overexposure brightness level (above which the image becomes saturated or "washed out") and an underexposure level (below which details disappear into the darkness). The dynamic range of a CCD is less than that of the human eye; for example, a human observer can often see both shadowed and unshadowed features in a scene illuminated by sunlight, whereas a CCD cannot capture details simultaneously in both the brightest and darkest parts of the scene (see Figure 1).

The present technique provides for compression of the dynamic range of brightness of an image focused on a CCD so that all or most parts of the image lie within the dynamic range of the CCD. When such compression is effected, the CCD output can be expected to show details in both the brightest and darkest parts of the scene.

In practice, compression of the dynamic range of brightness in an image must be accomplished through local darkening

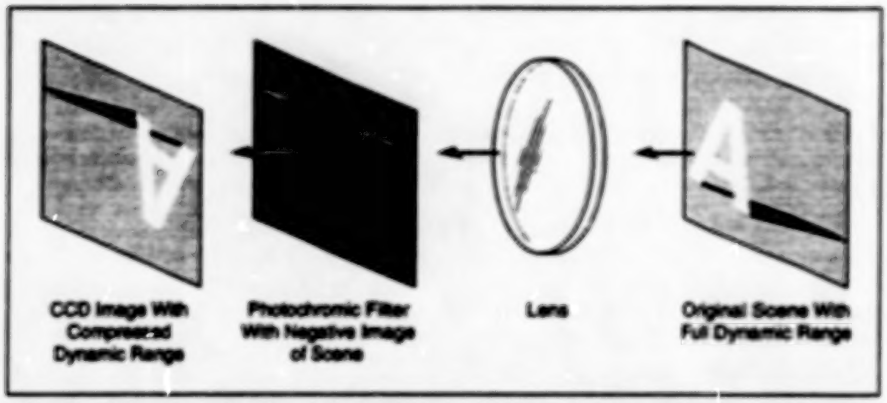
CCD Image With Compressed Dynamic Range
Photochromic Filter With Negative Image of Scene
Lens
Original Scene With Full Dynamic Range

Figure 2. A Photochromic Filter at the Image Plane becomes, in effect, a temporary photographic negative with a dynamic range somewhat less than that of the image. Therefore, the net image projected through the filter looks like the original scene, except that it has less dynamic range.

of the image, with greater darkening in brighter locations. Photochromic material exhibits the required greater darkening with exposure to brighter light. In the present technique, a photochromic filter is placed at (or immediately in front of) the CCD image plane, so that it becomes darkened in the bright areas of the image (see Figure 2). As a result, the light that passes through the photochromic filter forms the desired reduced-dynamic-range version of the image.

This work was done by Richard A. Volpe of Caltech for **NASA's Jet Propulsion Laboratory.** *Further information is contained in a TSP [see page 1].*

NPO-20254

Self-Checking Circuitry for Detecting Single-Event Latchups

A voting scheme would reveal anomalies in complex circuits with wide dynamic ranges.

NASA's Jet Propulsion Laboratory, Pasadena, California

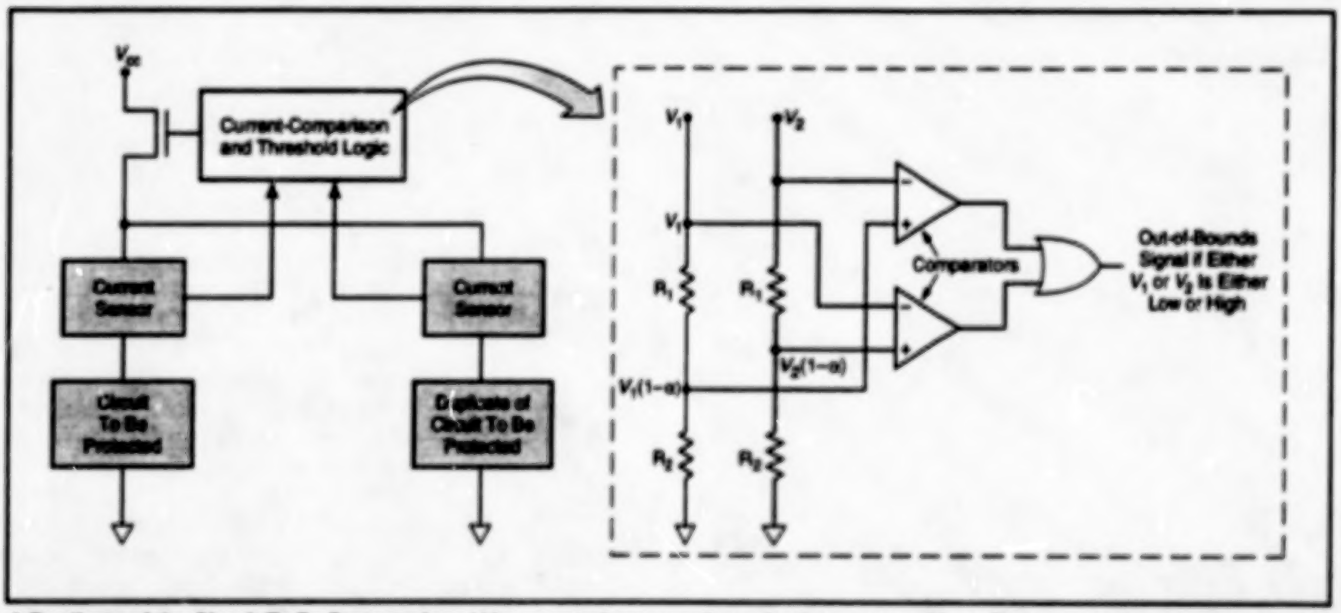

A Duplicate of the Circuit To Be Protected would be operated concurrently, under the same conditions. The currents drawn by the protected circuit and its duplicate would be indicated by V_1 and V_2. If either of V_1 or V_2 differed from the other by a fraction greater than $R_1/(R_1+R_2) = \alpha$, then the circuit would generate an "out-of-bounds" signal.

High-performance electronic circuits would incorporate self-checking features for detection of radiation-induced single-event latchups (SELs), according to a proposal. The basic SEL-detection scheme calls for redundant circuitry and a current-voting scheme similar to voting schemes that have been used to reveal malfunctions in other redundant systems. The redundancy and voting scheme could also be combined with other fault-tolerance features [e.g., for detection of single-event upsets (SEUs)].

As in some older schemes for detecting SEL and other anomalies, the proposed current-voting scheme would involve detection of operating current outside the normal range for a circuit to be protected. However, unlike in some older methods for detecting SEL, no attempt would be made to establish precise limits of normal operating current — limits that could be difficult if not impossible to establish for a complex circuit that normally operates over a wide dynamic range of current and/or is subject to radiation or to variations in temperature. Instead, one would build a duplicate of the circuit to be protected and would operate both circuits concurrently under the same nominal conditions, using comparator circuitry to detect differences between the currents drawn by the two circuits (see left side of figure). Each of the duplicate circuits would serve as a high-fidelity model of "normal" behavior for the other. "Normal" behavior would be defined ratiometrically; that is, in terms of a range, α, of allowable fractional difference between the currents (or corresponding voltages) in the two

duplicate circuits. Any excursion from the allowable range would be detected by the comparator circuitry, which would respond by triggering an alarm, shutdown, reset, or other appropriate corrective signal.

The current-voting scheme could be implemented, for example, by the current-comparison and threshold-logic circuitry shown on the right side of the figure. Potentials V_1 and V_2 are voltages representative of the currents flowing from a power supply (at potential V_{CC}) to each of two duplicate circuits. The values of R_1 and R_2 would be chosen so that $R_1/(R_1+R_2) = \alpha$. Thus, the left voltage divider (R_1,R_2) would provide comparison voltages V_1 and $V_1(1-\alpha)$, while the right voltage divider (R_1,R_2) would provide comparison voltages V_2 and $V_2(1-\alpha)$. Then the output of the upper comparator would go high if V_2 were less than $V_1(1-\alpha)$, whereas the output of the lower comparator would go high if V_1 were less than $V_2(1-\alpha)$. It is noted that in this scheme, it would not matter which voltage (V_1 or V_2) was the "normal" voltage; instead, if either voltage deviated from the other by a fraction $>\alpha$, the behavior would be deemed to be abnormal, causing the circuit to generate an "out-of-bounds" signal.

This work was done by Douglas W. Caldwell of Caltech for **NASA's Jet Propulsion Laboratory**. *Further information is contained in a TSP [see page 1].*

In accordance with Public Law 96-517, the contractor has elected to retain title to this invention. Inquiries concerning rights for its commercial use should be addressed to

Technology Reporting Office
JPL
Mail Stop 122-116
4800 Oak Grove Drive
Pasadena, CA 91109
(818) 354-2240

Refer to NPO-20143, volume and number of this NASA Tech Briefs *issue, and the page number.*

BLANK PAGE

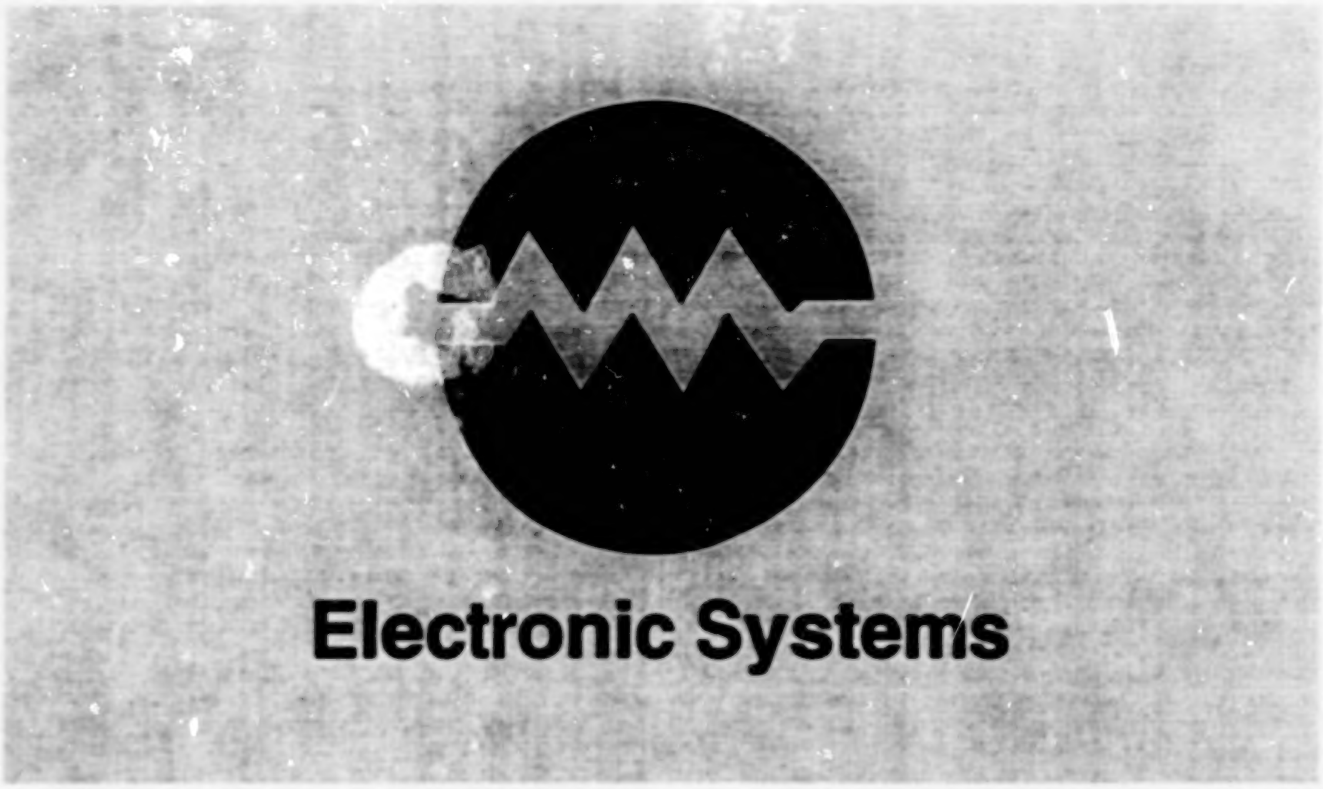

Electronic Systems

Hardware, Techniques, and Processes

15 Laser Doppler Velocimeter System for Use on Gas Turbines

16 "Smart" Optoelectronic Sensor System for Recognizing Targets

BLANK PAGE

Laser Doppler Velocimeter System for Use on Gas Turbines

The LDV transceiver has been ruggedized to withstand engine vibrations and noise.

Dryden Flight Research Center, Edwards, California

A laser Doppler velocimeter (LDV) system has been developed for use on practical gas-turbine engines. The system has been used to measure inlet and exhaust velocities on an F-100 EMD engine from an F-15 airplane (see Figure 1). To perform this work successfully, it was necessary to develop several novel subsystems, including a rugged LDV transceiver, a high-performance frequency-domain signal processor, and equipment for adding seed particles to the inlet and exhaust flows. In addition, it was necessary to provide for remote control of the system from a blockhouse at a distance of 30 m from the engine.

The LDV transceiver features a special ruggedized design: The main structural component of the transceiver was machined from a billet of aluminum, and all optics were hard-mounted on this component. This was necessary to enable the LDV transceiver to survive the intense vibrational and acoustical fields that surround a practical gas-turbine engine.

A 40-MHz Bragg cell provides frequency shifting for the LDV. The laser beam is generated by an argon-ion laser in the blockhouse and delivered to the LDV transceiver by a 30-m-long, single-mode, polarization-preserving optical fiber (see Figure 1). The intensity of the laser beam emerging from the end of the fiber-optic link in the LDV transceiver is monitored remotely; that is, from within the blockhouse. A second 30-m-long multimode optical fiber delivers the scattered light received from seed particles passing through the interferometric LDV probe volume to a photodetector in the blockhouse. This photodetector is a photomultiplier/preamplifier combination developed specially to perform at signal frequencies >120 MHz — well in excess of characteristic response frequencies of typical photodetectors in older LDV systems.

The frequency-domain signal processor, known as the Real-Time Signal Analyzer™ (RSA), was developed to provide an easy-to-operate, extremely capable processor of LDV signals. The RSA can perform up to 10^7 measurements per second on LDV signals and is thus capable of performing at rates well in excess of any expected data rates. Not only is the potentially noisy LDV signal measured in the frequency domain by use of discrete Fourier transforms, but the Doppler burst is also detected in the frequency domain, enabling operation at signal-to-noise ratios well below 0 dB. The output of the RSA is delivered to a laptop computer, where the results are displayed in real time and stored. All control over the RSA is exercised via this computer.

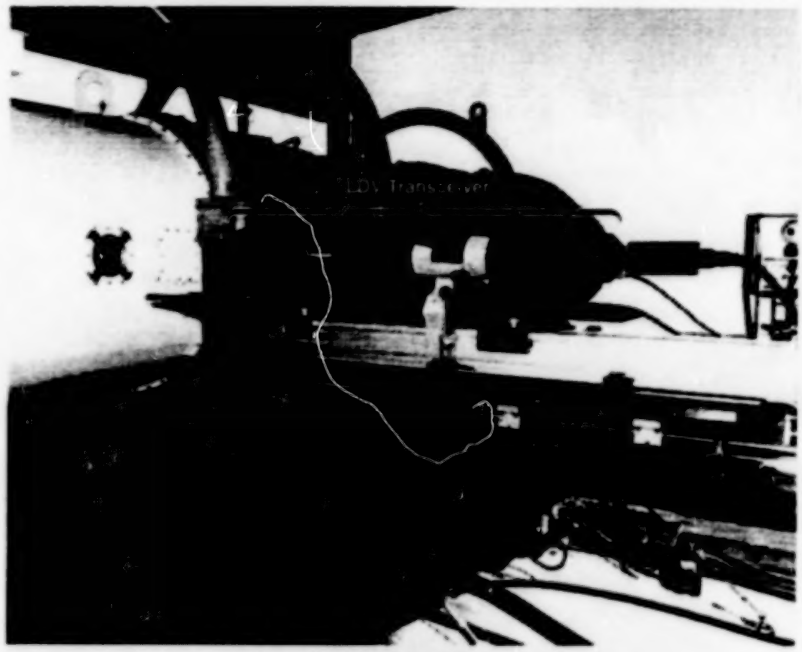

LDV TRANSCEIVER MOUNTED NEAR ENGINE

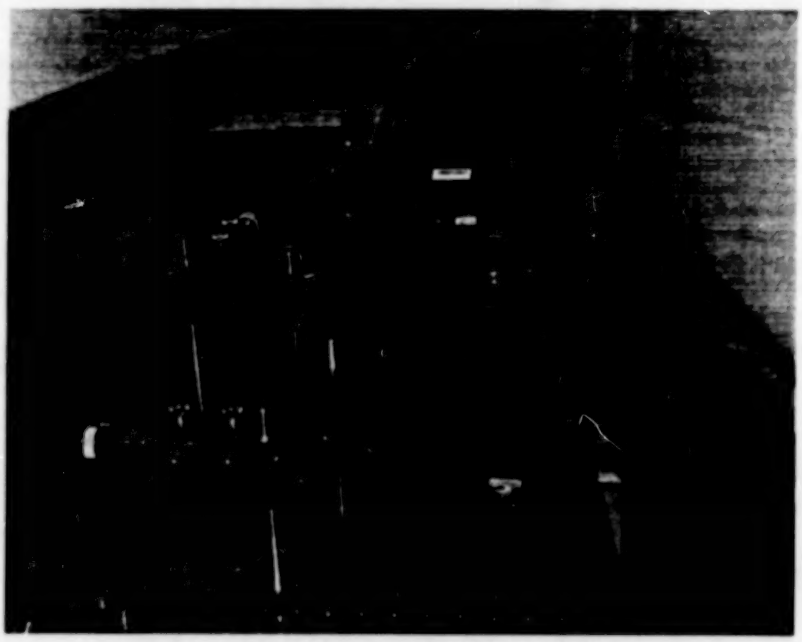

LASER AND ASSOCIATED OPTICS IN BLOCKHOUSE

Figure 1. The LDV System includes a rugged LDV transceiver mounted near the engine and connected via optical fibers to optical and electronic instrumentation in the blockhouse.

Two seeders were developed. One was an evaporation/condensation seeder that introduced a propylene glycol smoke, as a nonhazardous seeding material, into the inlet flow. This seeder was specially designed to minimize perturbation of the inlet flow and eliminate a possibility of introduction of foreign objects that could damage the engine. The other seeder — of the fluidized-bed type — introduced refractory seed particles into a moderate-pressure engine bypass airflow downstream of the

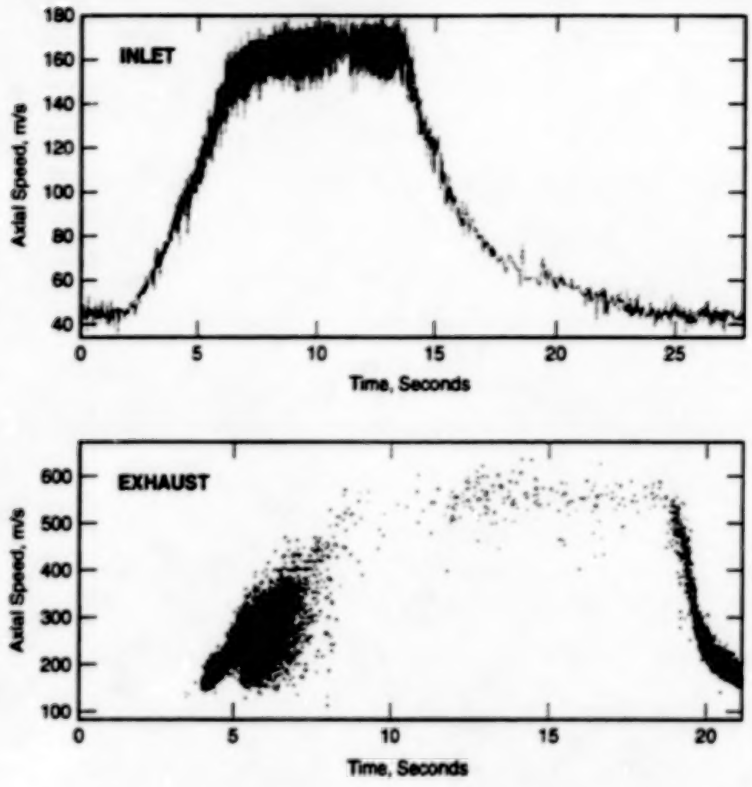

Figure 2. These **Plots Show Axial Speeds** in inlet and exhaust flows as measured by use of the LDV system during a transient from idle to full military power then back to idle.

engine to enable LDV measurement of the exhaust flow. Both seeders were required to provide copious amounts of seed to obtain adequate data rates at the high flow rates of a practical gas-turbine engine.

Figure 2 presents some results from a sample test run, showing inlet and exhaust axial speeds for a transient ramp from idle to full military power, then back to idle. The success in using this system to perform ground-based measurements raises the hope of accomplishing such measurements in flight on a practical aircraft in the future.

This work was done by Kimberly Ennix, Tim Conners, and Dean Webb of **Dryden Flight Research Center** *and Roger Rudoff, John Hanscom, Robert Shearrer, and William D. Bachalo of Aerometrics, Inc. Further information is contained in a TSP [see page 1].*

In accordance with Public Law 96-517, the contractor has elected to retain title to this invention. Inquiries concerning rights for its commercial use should be addressed to

Aerometrics, Inc.
755 N. Mary Avenue
Sunnyvale, CA 94086

Refer to DRC-98-08, volume and number of this NASA Tech Briefs *issue, and the page number.*

"Smart" Optoelectronic Sensor System for Recognizing Targets

Applications could include defense against missiles, medical imaging, and robotics.

NASA's Jet Propulsion Laboratory, Pasadena, California

The Viewing Imager/Gimballed Instrumentation Laboratory and Analog Neural Three-Dimensional Processing Experiment (VIGILANTE) is a "smart" optoelectronic sensor system that features ultrafast processing of image information for recognition and tracking of targets. VIGILANTE serves as a test bed for generic automatic-target-recognition (ATR) applications, with emphasis on demonstrating ATR capabilities for military defense against cruise missiles. Other applications for sensor systems derived from VIGILANTE could include medical imaging and machine vision for industrial robots and robotic vehicles.

VIGILANTE comprises two main subsystems (see figure). The VIGIL subsystem is an airborne telescope used to acquire image data for target-recognition experiments and to test novel passive and active focal-plane image sensors. The telescope will ultimately include a 15-cm Cassegrain unit, a gimballed mirror, and optical and electronic channels for multiband (infrared, visible, and ultraviolet) image sensors.

The ANTE subsystem is a prototype image-processing/target-recognition analog/digital computer system. The core computing engine in this system is a three-dimensional artificial neural network (3DANN) of a type described in "Neural-Network Modules for High-Speed Image Processing" (NPO-19881), *NASA Tech Briefs*, Vol. 21, No. 10 (October 1997), page 26. A 3DANN is a low-power-consumption digital/analog integrated-circuit module, about the size of a sugar cube, that can process data at a rate as high as 10^{12} operations per second. The integrated-circuit stack of a previous 3DANN was mated to an array of infrared sensors. The 3DANN in ANTE is a modified version of the previous 3DANN, denoted "3DANN-M." The modifications enable VIGILANTE to accept data from an image sensor of arbitrary size and format. More importantly, the 3DANN-M can be used to perform general convolution operations on image kernels as large as 64 × 64 pixels.

VIGILANTE is designed to make the most of whatever imagery is presented, whether that imagery be monochromatic, multispectral, still, or moving. For this purpose, the VIGILANTE processing architecture is modeled after the image-processing architecture of the human eye and brain. The VIGILANTE image-recognition process is divided into four stages: collection of images from sensors, generation of synthetic images that augment raw images with additional information, fusion of all images, and semantic interpretation of fused images. The use of synthetic images is consistent with the hypothesis that the brain uses synthetic imagery to analyze scenes by comparing corresponding pixels among images of various types. This hypothesis is equivalent to a "rich pixel" concept, according to which the brain becomes a data-fusion machine at

the pixel level, before it analyzes the entire scene in a semantic way.

By breaking complex image-recognition tasks into a series of regular operations, the VIGILANTE processing architecture maps image-recognition functions to a relatively small set of special-purpose electronic processing units that can implement a variety of algorithms. In particular, the special-purpose processing unit for generation of synthetic images (by such processes as spatial filtering, detection of motion, and identification of corresponding pixels in related images) is the 3DANN-M convolution device. Pixel-level fusion can be formed on such parallel-processing devices as single-instruction/multiple-data (SIMD) arrays. Relative to other functions, semantic analysis seldom presents a significant computational bottleneck and can ordinarily be performed by general-purpose computing hardware.

This work was done by Suraphol Udomkesmalee, Curtis Padgett, Wai-Chi Fang, and Steven Suddarth of Caltech for **NASA's Jet Propulsion Laboratory**. *Further information is contained in a TSP [see page 1].*
NPO-20357

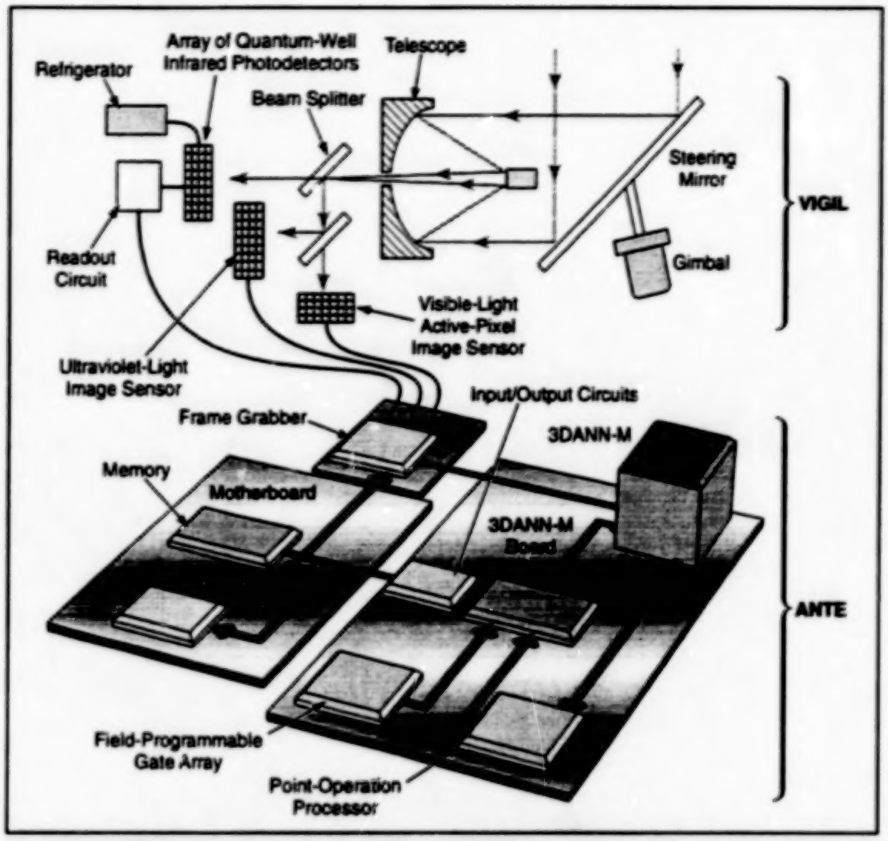

The **VIGILANTE System** comprises the VIGIL and ANTE subsystems. VIGIL includes an integrated optical system wherein incoming light is split by wavelength and directed to image sensors in three wavelength bands. ANTE contains a 3DANN, a point-operation processor, and ancillary circuits, all acting together to perform ATR functions in real time.

BLANK PAGE

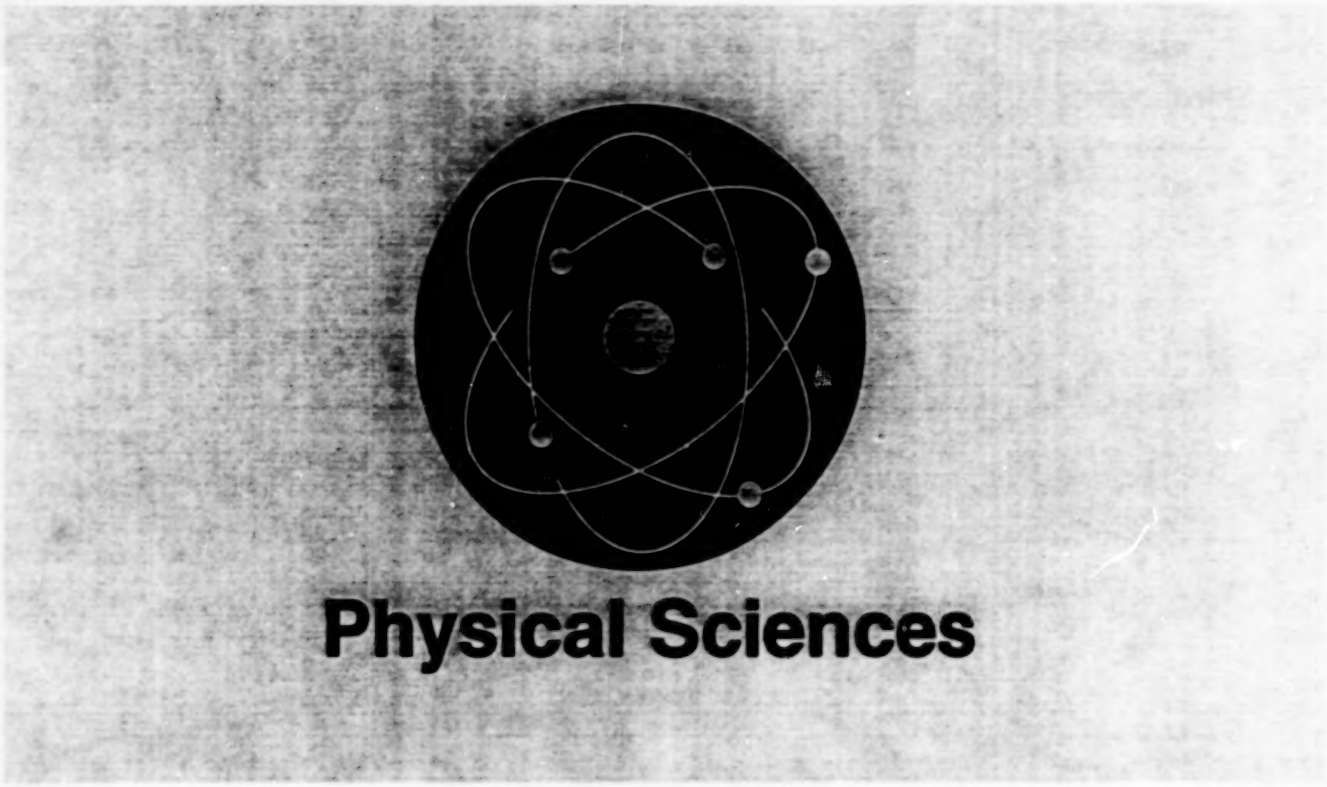

Physical Sciences

Hardware, Techniques, and Processes

21 Voltage-Tunable Surface-Plasmon Band-Pass Optical Filters
22 Coherent Gradient Sensing for Measuring Curvature
23 Microwave-Heating Technique for Batch Processing
24 Easy-to-Use High-Temperature Strain-Sensor Systems
25 Miniature Electron Microscopes Without Vacuum Pumps
26 Miniature Microscope Without Lenses
27 Semimonolithic Cavities for Optical Frequency Conversion
27 Microlenses for Calibrating Phase Doppler Particle Analyzers

BLANK PAGE

Voltage-Tunable Surface-Plasmon Band-Pass Optical Filters

Efficiencies would exceed those of previously developed liquid-crystal tunable filters.

NASA's Jet Propulsion Laboratory, Pasadena, California

Voltage-tunable optical band-pass filters based on surface plasmon waves have been proposed. These filters would function at both visible and infrared wavelengths. Whereas liquid-crystal tunable optical filters now on the market exhibit efficiencies of 20 percent or less, theoretical calculations predict that the efficiencies of the proposed tunable surface-plasmon filters could exceed 60 percent in some cases.

Figure 1 schematically illustrates one of two types of the proposed filters. A thin film of a suitable electro-optical material (for example, a liquid crystal) would be sandwiched between two high-index-of-refraction prisms coated with thin metal films at the prism/electro-optical-film interfaces. If p-polarized white light were to impinge on this device at a certain angle (denoted the surface-plasmon angle), then the energies of some of the incident photons would be converted into collective motions of free electrons in the upper metal film. Because of the thinness of the electro-optical film, the optical field would penetrate the film and excite the same collective motion of electrons in the lower metal film. As a result, light would be transmitted in the sense that it would be re-radiated from the bottom. Only the photons at the surface-plasmon resonance frequency could generate surface plasmon waves and could thereby be coupled through the thickness to contribute to the transmitted light; consequently, the transmitted light would be colored.

The surface-plasmon resonance frequency would depend on the indices of refraction of both the metal film and the liquid crystal or other electro-optical material. If a voltage were applied to control the index of refraction of the electro-optical material, then the voltage would control surface-plasmon resonance frequency and thus the spectrum of the transmitted light.

For example, theoretical calculations were performed for a device like that of Figure 1 comprising TiO_2 prisms with 45° angles, silver films 35 nm thick, and a 150-nm-thick electro-optical film made of a recently developed liquid crystal, the index of refraction of which can be made to shift as much as 0.5. According to the calculations, with no

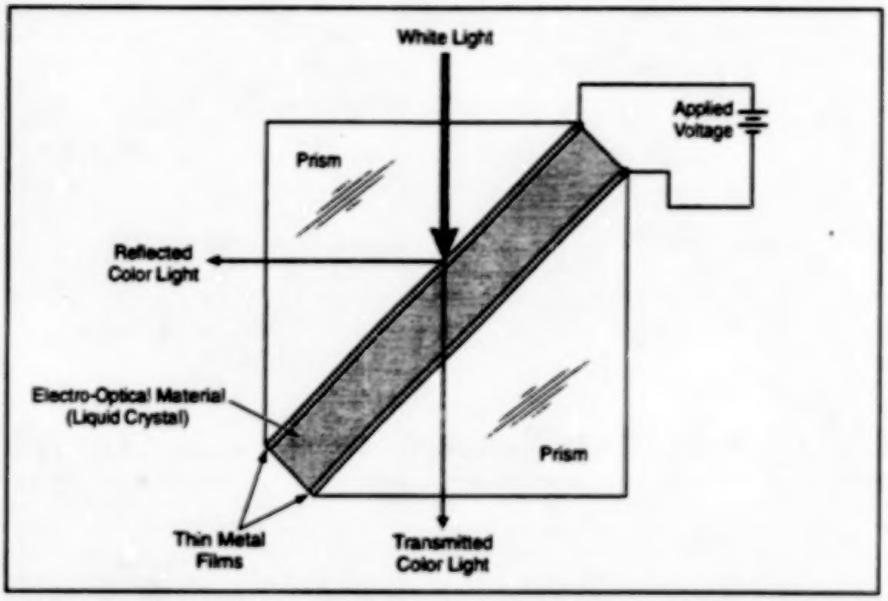

Figure 1. The Applied Voltage Would Alter the Index of Refraction of the electro-optical material, thereby altering the surface-plasmon resonance frequency and shifting the spectrum of transmitted light.

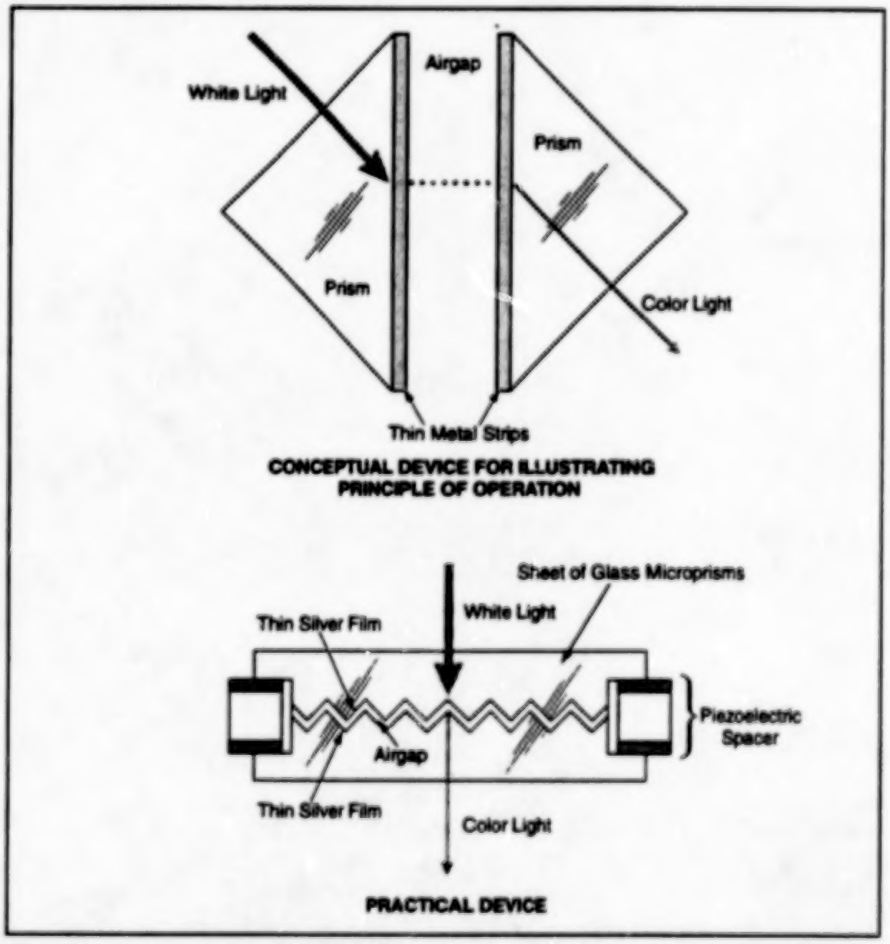

Figure 2. The Airgap Would Be Varied to alter the surface-plasmon resonance frequency and thereby shift the spectrum of transmitted light.

voltage applied to the silver films, the device would exhibit peak transmission at a wavelength of 450 nm (blue), with an efficiency of 62 percent. With enough voltage applied to shift the index of refraction by 0.5, the peak of the transmission spectrum would be shifted to 650 nm (red), and the efficiency would be 70 percent.

If a metal other than silver were used, the device could be made to work in infrared light. For example, if the silver films in the device described in the preceding paragraph were replaced with potassium films, then the wavelength of peak transmission could be made to range from 1,050 to 1,700 nm.

A proposed tunable surface-plasmon optical filter of the second type would also include prisms partly coated with thin metal films (see Figure 2), but there would be no electro-optical film with a voltage applied to control its index of refraction. Instead, an airgap would be left between the metal films, and the distance between the prisms would be varied to vary the airgap and thereby vary the surface-plasmon resonance frequency. A practical device of this type could be made from sheets of microprisms, with piezoelectric spacers for varying the airgap.

This work was done by Yu Wang of Caltech for **NASA's Jet Propulsion Laboratory**. *Further information is contained in a TSP [see page 1].*

In accordance with Public Law 96-517, the contractor has elected to retain title to this invention. Inquiries concerning rights for its commercial use should be addressed to

Technology Reporting Office
JPL
Mail Stop 122-116
4800 Oak Grove Drive
Pasadena, CA 91109
(818) 354-2240

Refer to NPO-19988, volume and number of this NASA Tech Briefs *issue, and the page number.*

Coherent Gradient Sensing for Measuring Curvature

This is a full-field, real-time, noncontact optical technique.

NASA's Jet Propulsion Laboratory, Pasadena, California

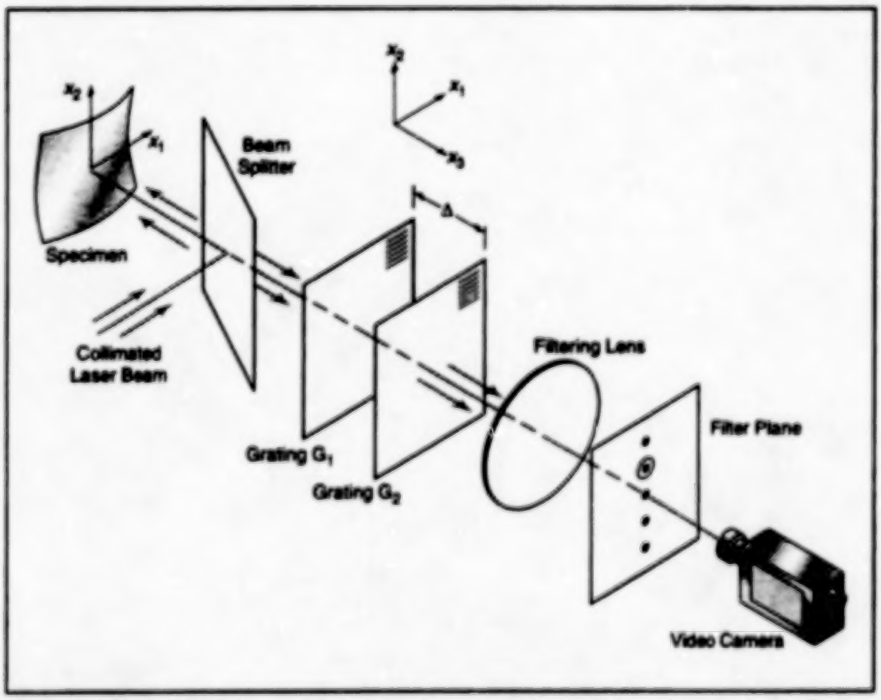

Figure 1. A Typical CGS Apparatus is set up to measure the curvature of a specularly reflective specimen.

Coherent gradient sensing (CGS) is a diffraction-based, noncontact optical technique for measuring the slight curvature of a nearly flat thin film or specimen surface. CGS is especially useful for measuring curvatures of micromechanical structures and of thin films in electronic devices, to enable the determination of stresses in, and mechanical properties of, such structures and films. CGS is a full-field, real-time technique: Unlike in some other techniques, it is not necessary to acquire images of the specimen surface at different times under different conditions of curvature, nor is it necessary to scan a narrow beam of light over the surface; instead, CGS yields data on curvature over the entire surface area of interest, in as little time as it takes to acquire, digitize, and process a video image. Moreover, CGS is insensitive to rotation or displacement of the specimen.

Figure 1 schematically illustrates a reflection-mode CGS optical setup. A coherent, collimated laser beam is directed onto a specularly reflective specimen via a beam splitter. The reflected beam passes through the beam splitter, then through two identical high-density (40 lines/mm) Ronchi gratings separated by a distance Δ. A lens spatially filters the portions of light diffracted to various orders to form distinct diffraction spots on a filter plane. An aperture is placed in the filter plane to select a diffraction order of interest and reject other orders. The order of interest is then imaged on the focal plane of a video camera. The video image is digitized and processed to extract information on the curvature of the specimen surface.

Suppose that the grating lines are oriented along the x_1 axis. Figure 2 illustrates the formation of the first few diffraction orders by each Ronchi grating, and the formation of some of the resulting images on the filter plane. The reflected wavefront incident on Ronchi grating G_1 is diffracted into wavefronts E_1, E_0, and E_{-1}, among others, these orders corresponding to diffraction orders 1,0, and −1, respectively. (For the sake of simplicity, only these orders are shown, though many others could be present.) Each of these wavefronts is diffracted by Ronchi grating G_2, yielding wavefronts $E_{1,1}$ through $E_{-1,-1}$, among others. Various sets of parallel diffracted beams are combined by the filtering lens to form diffraction spots D_1, D_0, and D_{-1}, among others.

The net effect of the gratings is a lateral (in this case, along x_2) shift or "shearing"

of the incident wavefront, leading to the formation of interference fringes. The fringe pattern has been analyzed theoretically, using the simplifying approximations that the wavefront (and thus the specimen) is nearly flat and that diffraction angles are small. The analysis reveals that the curvature of the specimen surface can be obtained from the CGS interference-fringe pattern via the equation

$$\kappa_{\alpha\beta} = \frac{p}{2\Delta}\left(\frac{\partial n^{(\alpha)}(x_1, x_2)}{\partial x_\beta}\right)$$

where $\alpha = 1$ or 2, $\beta = 1$ or 2, $\kappa_{\alpha\beta}$ is the curvature tensor, p is the grating pitch, and $n^{(\alpha)}$ denotes the cardinal number of a fringe observed in shearing along the x_α direction.

This work was done by Ares J. Rosakis, Raman P. Singh, Elzbieta Kolawa, and Nicholas R. Moore, Jr., of Caltech for **NASA's Jet Propulsion Laboratory.** *Further information is contained in a TSP [see page 1].*

In accordance with Public Law 96-517, the contractor has elected to retain title to this invention. Inquiries concerning rights for its commercial use should be addressed to

Technology Reporting Office
JPL
Mail Stop 122-116
4800 Oak Grove Drive
Pasadena, CA 91109
(818) 354-2240

Refer to NPO-20189, volume and number of this NASA Tech Briefs *issue, and the page number.*

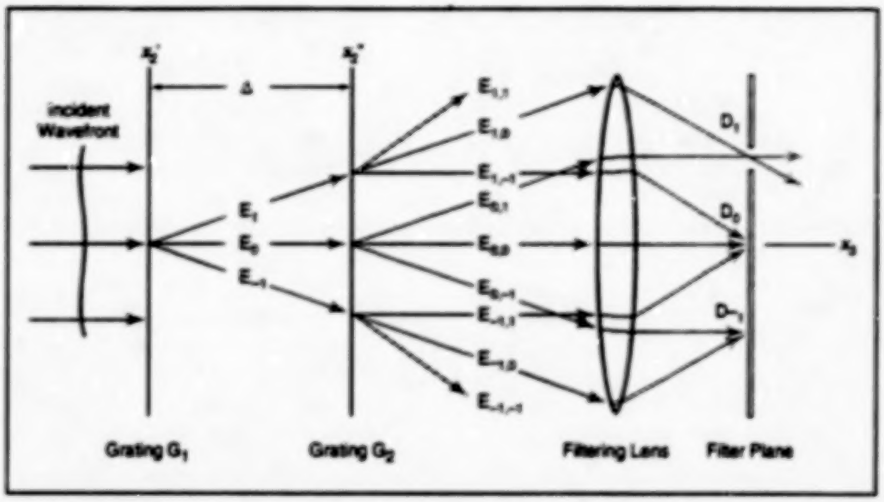

Figure 2. Diffraction, Interference, and Spatial Filtering are utilized in CGS to obtain an image containing interference fringes that are indicative of the curvature of the specimen.

Microwave-Heating Technique for Batch Processing

Multiple samples are positioned to exploit symmetry in cavity modes.

NASA's Jet Propulsion Laboratory, Pasadena, California

A microwave-heating technique provides for batch processing of multiple, identically sized and shaped samples of the same material. The technique involves (1) excitation of a symmetrical electromagnetic mode or modes in a symmetrical microwave cavity and (2) positioning the samples symmetrically in the cavity so that all samples are exposed to the same electromagnetic-field conditions and thus the same heating conditions. Typically, electromagnetic mode(s) and the part for mounting the samples are chosen to maximize the heating effect and make it as nearly spatially uniform as possible.

For example, the figure illustrates an application of the technique to microwave heating of N (in this case, $N = 8$) rod samples in a circular cylindrical cavity of radius r_0. In this case, the microwave excitation is supplied in the TM_{020} mode, in which the electromagnetic field depends on radial position r but is independent of azimuthal angle θ and of axial position z. Then for identical treatment, the samples should be positioned in the cavity at the same radius at equal angular intervals $\Delta\theta = 2\pi/N$.

When the cavity is empty, the magnitude of the electric field attains maxima at

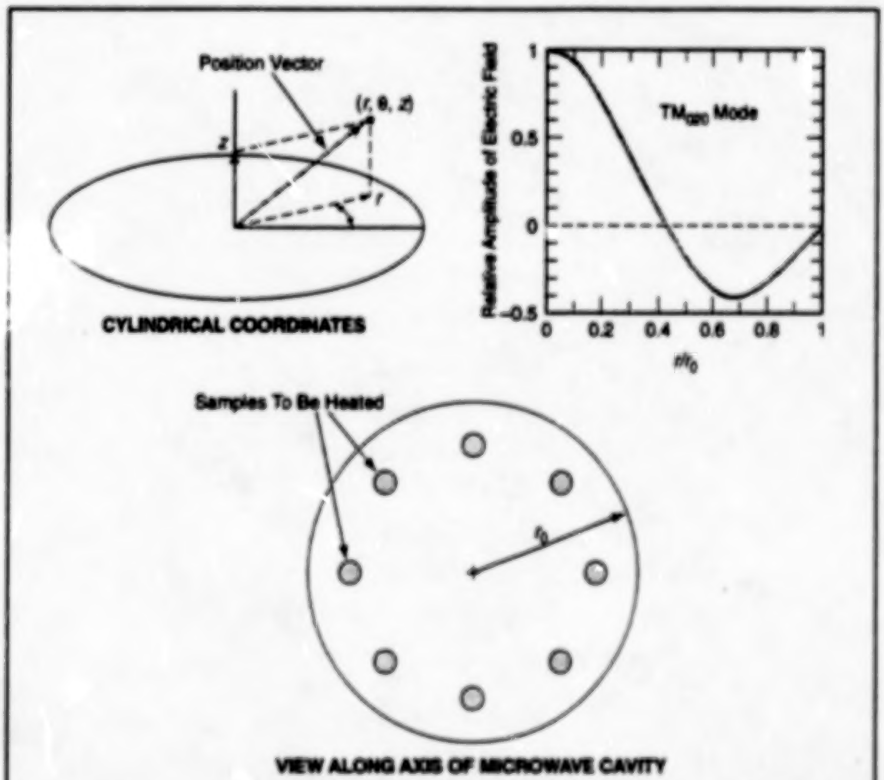

The Samples Are Positioned at equal angular intervals at a radius chosen to minimize nonuniformity and maximize coupling to the electric or magnetic field in the TM_{020} mode. Other modes with exploitable symmetries could also be used.

$r = 0$ and at the cylindrical surface $r/r_0 = 0.6941$, while the magnitude of the magnetic field attains maxima at the cylindrical surfaces $r/r_0 = 0.3336$ and $r/r_0 = 0.9658$. To a first approximation, assuming that the samples perturb the electromagnetic field minimally, the samples should be positioned on one of these surfaces to maximize heating: If the samples are electrically resistive or nonconductive, then they should be positioned at $r/r_0 = 0.6941$ for maximum coupling to the electric field; if the samples are highly electrically conductive, then they should be positioned at $r/r_0 = 0.3336$ or $r/r_0 = 0.9658$ for maximum coupling to the magnetic field.

Of course, the samples can be expected to perturb the electromagnetic field, the degree of perturbation increasing with the size of the samples. In the absence of an exact theory for the effect of the samples on the electromagnetic field, it could be necessary to conduct experiments to determine the radial position for maximum and/or most nearly uniform heating.

The same principle can be applied to microwave heating of multiple spherical or disk-shaped samples. In this case, the samples should not only be mounted at the same radius and at equal angular intervals but should also be mounted at the axial-mid-length plane to minimize nonuniformity of heating by enforcing symmetry with respect to z.

This work was done by Martin Barmatz and Henry W. Jackson of Caltech for **NASA's Jet Propulsion Laboratory**. *Further information is contained in a TSP [see page 1].*

In accordance with Public Law 96-517, the contractor has elected to retain title to this invention. Inquiries concerning rights for its commercial use should be addressed to

Technology Reporting Office
JPL
Mail Stop 122-116
4800 Oak Grove Drive
Pasadena, CA 91109
(818) 354-2240

Refer to NPO-19771, volume and number of this NASA Tech Briefs *issue, and the page number.*

Easy-to-Use High-Temperature Strain-Sensor Systems

Pd/Cr strain gauges are prestabilized and precalibrated under controlled conditions.

Lewis Research Center, Cleveland, Ohio

Easy-to-use high-temperature strain-sensor systems based on strain gauges made from Pd/Cr-alloy wires have been developed. These systems include strain-gauge units comprising Pd/Cr wires bonded to high-temperature metal-alloy shims by flame spraying of ceramic materials. Optionally, a strain-gauge unit can be supplied alone, but ordinarily, it is delivered as part of a system that also includes an integral, weldable-terminal high-temperature cable and a bridge-circuit-completion module at the cool end of the cable (see figure).

Strain gauges made from Pd/Cr-alloy wires, and techniques and materials used to fabricate them, have been described in a number of previous articles in *NASA Tech Briefs*. Pd/Cr-wire strain gauges can be used to measure static strains at temperatures up to 1,400 °F (760 °C). However, the successful use of these strain gauges entailed considerable difficulty prior to the development of the present systems. This is because in order to realize the full potential of Pd/Cr strain gauges, it is necessary to adhere strictly to installation, stabilization (heat treatment), and calibration procedures unlike those of conventional practice for lower-temperature strain gauges. The major advantage afforded by the development of present systems does not lie in any single fundamental physical concept, but, rather in the establishment of the practice of performing all critical steps in a controlled laboratory environment at the factory, before use in the field.

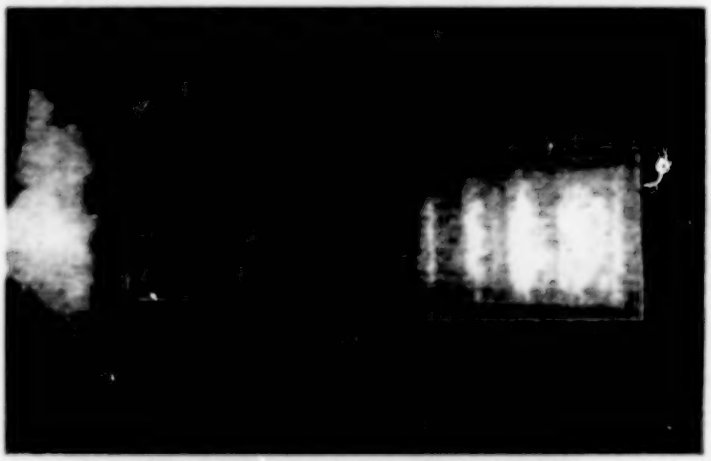

Weldable Strain-Gauge Unit With Terminal

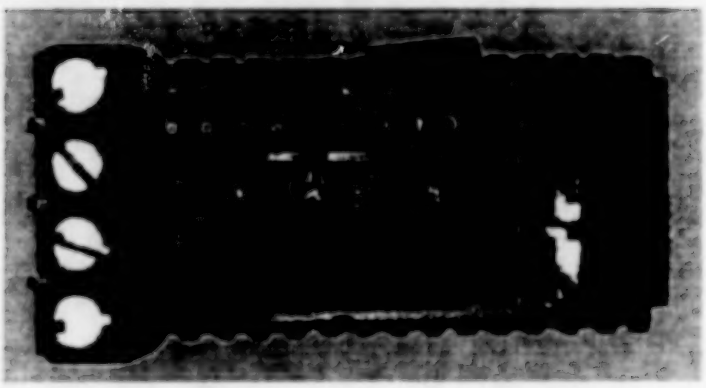

Bridge-Circuit-Completion Module

A Strain-Measurement System comprises a strain-gauge unit, a cable, and bridge-circuit-completion module. All critical steps in fabrication, installation, stabilization, and calibration are performed under controlled conditions prior to delivery of the system.

The prefabrication of strain-gauge units containing Pd/Cr wires bonded to shims overcomes the installation difficulty. The critical flame-spraying steps are performed under controlled factory conditions, rather than by the end user. Each unit includes a margin of shim material around its periphery; the margin can be used to attach the strain-gauge to a test structure (a structure on which strain is to be measured) by ordinary spot-welding at the end-use site.

Prior to calibration, each strain-gauge unit is prestabilized by heating at a temperature of 1,440 °F (782 °C) for 50 hours. Care is taken to maintain this temperature within a narrow margin of error; underheating causes changes in electrical resistance to be smaller than expected, while even momentary overheating destroys a temperature-compensation feature. In other words, both underheating and overheating introduce calibration errors.

To prepare for calibration, a strain-gauge unit is tack-welded to a bar of the same material on which it is to be used to measure strain. Strain readings are taken at temperature intervals spanning the full test temperature range, using a calibrated ballast (bridge-completion) resistor inserted in the bridge-circuit-completion module. If necessary, the calibration procedure is repeated with different bridge-completion resistors until a satisfactory calibration curve is obtained.

Once calibration has been performed in the laboratory, the strain-measurement system (including the final chosen bridge-completion resistor) is ready for use. The strain-gauge unit can be spot-welded to a test structure, and the system plugged into any common strain-measuring instrument and operated without need for further stabilization or calibration.

This work was done by J.F. Lei of **Lewis Research Center** *and S. P. Whuk, Jr., and V. P. Whuk of Hitec Products, Inc. Further information is contained in a TSP [see page 1].*

Inquiries concerning rights for the commercial use of this invention should be addressed to NASA Lewis Research Center, Commercial Technology Office, Attn: Tech Brief Patent Status, Mail Stop 7–3, 21000 Brookpark Road, Cleveland, Ohio 44135. Refer to LEW-16572.

Miniature Electron Microscopes Without Vacuum Pumps

Self-contained, microfabricated devices with short working distances, enable operation in air.

NASA's Jet Propulsion Laboratory, Pasadena, California

The proposed electron microscope would function without the need for external vacuum pumps and thus have a significant reduction in size, mass, and power consumption, as compared to conventional (vacuum-pump-equipped) electron microscopes now used in many laboratories. These devices could be used for both imaging as well as chemical-composition determination, in laboratory and field applications. There may be a significant potential market for these devices in applications now served by conventional scanning and transmission electron microscopes in physical and biological sciences, engineering, medicine, and chemistry.

Because the proposed devices could operate in air, it would not be necessary to prepare specimens for examination in vacuum; this is a decisive advantage in situations in which vacuum or the preparation process could damage specimens (e.g. biological specimens). Vacuum pumps are used in conventional electron microscopes because vacuum enables the lossless propagation of electrons over required distances. In the presence of a gas (e.g., air), electrons propagate over short distances, with loss of kinetic energy. In the operation of the proposed devices, working distances to specimens would be made small enough to limit attenuation of electrons to acceptable levels. The spatial resolution is determined primarily by the properties of the electron-transparent, atmosphere isolation membrane that encapsulates the electron column. The best achievable spatial resolution is expected to be at the micron level, whereas conventional electron microscopes give nanometer resolutions. Nevertheless, the advantages may outweigh the loss of resolution in many applications.

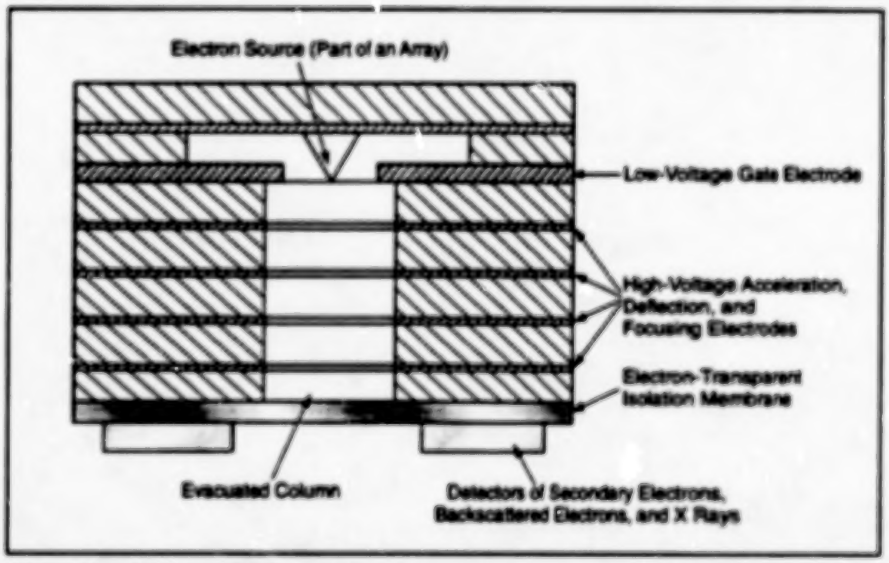
Electron Source (Part of an Array)
Low-Voltage Gate Electrode
High-Voltage Acceleration, Deflection, and Focusing Electrodes
Electron-Transparent Isolation Membrane
Evacuated Column
Detectors of Secondary Electrons, Backscattered Electrons, and X Rays

A Pumpless Miniature Electron Microscope would be made by microfabrication techniques based largely on micromachining of silicon. The stacked parts would be assembled in vacuum, following a wafer-to-wafer-bonding approach.

In addition to the advantages mentioned above, the proposed electron microscopes offer the great advantage of mass-producibility at relatively low cost by microfabrication techniques established for silicon micromachining. The fabrication process for the proposed electron microscopes would also exploit the recent development of low-voltage, low-power arrays of field-emission electron sources, the miniaturization of high-voltage electronics, and the development of devices that can detect secondary electron emission in the presence of gases.

A typical microfabricated electron microscope column is expected to be a few millimeters thick and about a centimeter square. The evacuated column will consist of a stack of microfabricated chips with metal-film apertures that will serve as electrodes for acceleration, deflection, and focusing of the electrons

(see figure). The electron sources will either be an array of thermionic or field emitters, depending on the vacuum level maintained by an integral ion pump (not shown). Although typical field-emission sources require ultra-high vacuum [~10^{-10} torr] for operation, the development of diamond-based field emitters promises much less stringent vacuum requirements [as low as 10^{-4} torr] for operation.

The key to the self-contained, atmospheric operation is the electron-transparent membrane that encapsulates the electron column. Recently, high-quality thin films of materials such as silicon nitride, boron nitride, and diamond have been developed. These materials have a low average atomic number and are mechanically very robust. Thus extremely thin films of these materials offer low electron attenuation with the ability to withstand over one atmosphere of differential pressure.

The detectors for the electron microscope will be mounted outside the encapsulating membrane. These detectors will measure fluxes of characteristic x-rays, backscattered electrons and secondary electrons via gas ionization, emitted by the sample in response to the primary electron irradiation.

This work was done by Thomas George of Caltech for **NASA's Jet Propulsion Laboratory**. *Further information is contained in a TSP [see page 1].*

NPO-20335

Miniature Microscope Without Lenses

Focusing optics would be supplanted by a microchannel filter and electronic image sensor.

NASA's Jet Propulsion Laboratory, Pasadena, California

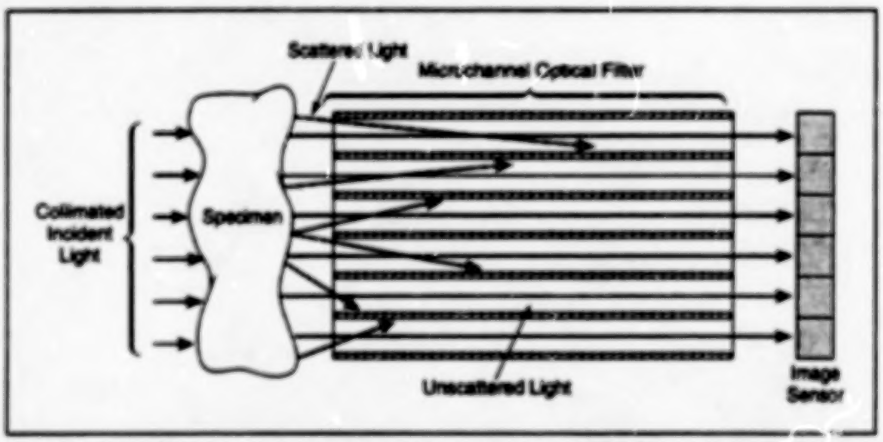

This Miniature Microscope would not contain any lenses or other focusing optics. Focusing would not be necessary because the specimen would be imaged in collimated light on an electronic image sensor with microscopic pixels.

In a proposed optical microscope, the focusing optics of a conventional microscope would be supplanted by a combination of a microchannel filter and an advanced electronic image sensor. Elimination of focusing optics would eliminate the need for the time-consuming focusing operation, making it possible to examine different specimens in faster succession. Elimination of the focusing optics would also result in a smaller, lighter instrument.

Electronic image sensors with pixel sizes of several microns have been developed. During the next few years, pixel sizes in advanced image sensors may be reduced to <1 μm — close to the limit of resolution of a conventional microscope with focusing optics. In that case, and if it were possible to effect a one-to-one mapping from a point on a specimen to a pixel in such an image sensor, then the electronic output of the sensor would contain image information equivalent to that from a microscope.

The desired one-to-one mapping could be obtained by use of conventional optics to focus an image of the specimen onto the image sensor, but in this case, one seeks to avoid the use of focusing optics. Instead, according to the proposal, the following would be done: The specimen would be illuminated with highly collimated light (e.g., laser light) aimed through the specimen and toward the image sensor (see figure). Assuming that the specimen were thin enough to be partially transparent but were also highly scattering, the unscattered portion of the incident light would continue to travel along the direction of incidence, and some would be scattered in other directions.

A narrow-angle filter — a filter capable of absorbing the scattered light — would be placed between the specimen and the sensor. Such a filter could be constructed as a plate or block of opaque material with straight microchannels; more specifically, parallel microscopic-cross-section holes much longer than they are wide. The microchannels should be positioned and dimensioned so that each one is registered with a pixel on the image sensor.

The scattered light would be absorbed on the walls of the holes, and only the unscattered light would pass through. Therefore, the light arriving at each pixel on the sensor would have traveled along a straight line from a corresponding location on the specimen. Given the parallelarity of the holes and of all the optical paths in a collimated beam of light, the geometric relationship among the pixels would match that of the corresponding location in the specimen. Thus, the desired one-to-one mapping would have been effected.

This work was done by Yu Wang of Caltech for **NASA's Jet Propulsion Laboratory**. *Further information is contained in a TSP [see page 1].*

In accordance with Public Law 96-517, the contractor has elected to retain title to this invention. Inquiries concerning rights for its commercial use should be addressed to

Technology Reporting Office
JPL
Mail Stop 122-116
4800 Oak Grove Drive
Pasadena, CA 91109
(818) 354-2240

Refer to NPO-20218, volume and number of this NASA Tech Briefs issue, and the page number.

Semimonolithic Cavities for Optical Frequency Conversion

Most advantages of monolithic cavities would be retained and most disadvantages eliminated.

NASA's Jet Propulsion Laboratory, Pasadena, California

Semimonolithic resonant structures external to lasers have been proposed for use in optical frequency-conversion applications — for example, doubling the frequencies of laser beams. These structures would offer most of the advantages, without most of the disadvantages, of monolithic resonant cavities.

In contradistinction with discrete external cavities (that is, external cavities that are assemblies of discrete optical components), monolithic external cavities offer advantages of lower overall intracavity losses, no dispersion-induced mismatches, mechanical stability with consequent frequency stability, compactness, and lower overall cost. The disadvantages of monolithic cavities include vulnerability to manufacturing errors, lack of any degree of freedom for alignment, potential for difficulty in changing cavity lengths for resonance frequency locking, and, in some applications, unavailability of nonlinear crystals that are large enough.

A typical semimonolithic structure ("cavity") of the proposed type would include a nonlinear optical crystal fitted with optical components of glass or other suitable linear optical material on both ends (see figure). The glass chosen for this application must have an index of refraction as close as possible to that of the nonlinear crystal. The curved end mirrors of the cavity ("cavity mirrors," for short) would not be fabricated on the nonlinear crystal as in a monolithic cavity; instead, the cavity mirrors would be fabricated on the glass endpieces. The second-harmonic output could be extracted from the cavity through one of the cavity mirrors or through a dichroic beam splitter.

In a monolithic cavity, if any error occurs in fabrication of the cavity-mirror surfaces, or if the apices of these curved surfaces are not exactly coaligned, then the entire piece of nonlinear material must be discarded or completely reworked. In a semimonolithic cavity like the one proposed here, one could replace the glass endpieces or make small corrections on them. The polishing and coating characteristics of optical glasses and the techniques for fabricating mirror surfaces on them are well known. Thus, the fabrication of cavity mirrors on glass for the proposed cavity could be accomplished more reliably and cheaply than can fabrication of the same mirrors on an exotic nonlinear crystal for a monolithic cavity.

In the semimonolithic cavity, there would be some limited freedom to adjust the alignment of the cavity mirrors by slightly adjusting the positions and orientations of the glass endpieces before bonding them in place. The effective optical length of the cavity could be adjusted by applying an electric field to the nonlinear material, provided that the material was accessible in the position and orientation suitable for that purpose. Alternatively, prior to entering the resonant cavity, the laser beam could be bounced off a translation mirror that was piezoelectrically or otherwise adjustable. In thus freeing the cavity designer from limitations on the available size of the nonlinear crystal, the semimonolithic cavity would offer a major advantage.

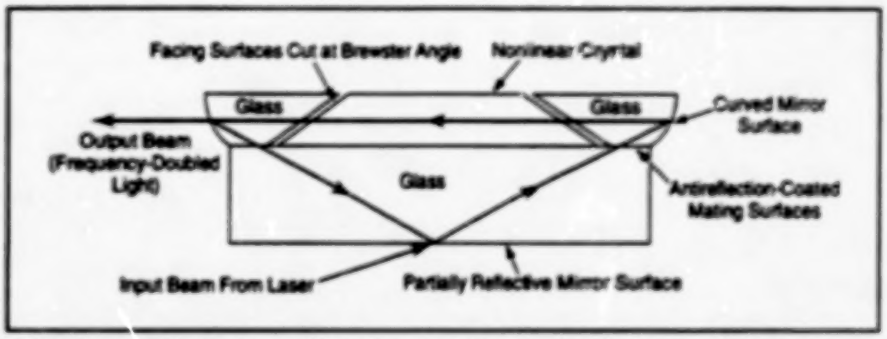

A Semimonolithic Cavity would cost less than does a monolithic cavity of equal capability. Unlike a monolithic cavity, it would be somewhat adjustable.

One disadvantage of the semimonolithic cavity would lie in the potential for optical losses that occur at the multiple surfaces traversed by the laser beam. Some of these surfaces could be antireflection-coated to reduce losses. The polished surfaces at the ends of the nonlinear crystal and the facing surfaces of the glass blocks could be formed at the Brewster angle to reduce losses further.

This work was done by Hamid Hemmati of Caltech for **NASA's Jet Propulsion Laboratory** *and funded under the AITP Program. Further information is contained in a TSP [see page 1].*

In accordance with Public Law 96-517, the contractor has elected to retain title to this invention. Inquiries concerning rights for its commercial use should be addressed to

Technology Reporting Office
JPL
Mail Stop 122-116
4800 Oak Grove Drive
Pasadena, CA 91109
(818) 354-2240

Refer to NPO-19789, volume and number of this NASA Tech Briefs *issue, and the page number.*

Microlenses for Calibrating Phase Doppler Particle Analyzers

Microlens devices give repeatable results and are small, easy to use, and relatively inexpensive.

Lewis Research Center, Cleveland, Ohio

Simple optical devices called "scattering reticles" have been invented for calibrating Phase Doppler Particle Analyzers (PDPAs), which are optical instruments that analyze scattered light to determine the sizes and velocities of droplets. A scattering reticle comprises a polymeric plano-convex microlens, typically with a diameter of about 60 μm, on a glass substrate about 4 mm thick. In operation, a three-axis positioning stage is used to hold the substrate and move the

microlens into the intersection of laser beams that defines the probe volume of a PDPA. The PDPA collects and analyzes the light scattered from the microlens.

Heretofore, PDPAs have been calibrated by use of droplet generators, which are difficult to use, are unreliable, and do not give repeatable results. Scattering reticles are easy to use, are small and inexpensive in comparison with droplet generators, and exhibit a high degree of repeatability.

To be useful for calibrating a PDPA, an optical device must scatter light in a manner similar to that of the droplets to be observed by the PDPA.

Ideally, the microlens on a scattering reticle should be hemispherical, but small deviations from hemisphericity are permissible.

Typically, a PDPA responds to light scattered by a microlens in the same way as to light scattered by droplets with a monodisperse size distribution. Scattering reticles with microlenses have been tested on two PDPAs, yielding results that were in agreement.

This work was done by Edward A. Hovenac of NYMA, Inc., and Steven James Bever of Wabash College for **Lewis Research Center**. *Further information is contained in a TSP [see page 1].*

Inquiries concerning rights for the commercial use of this invention should be addressed to NASA Lewis Research Center, Commercial Technology Office, Attn: Tech Brief Patent Status, Mail Stop 7–3, 21000 Brookpark Road, Cleveland, Ohio 44135. Refer to LEW-16350.

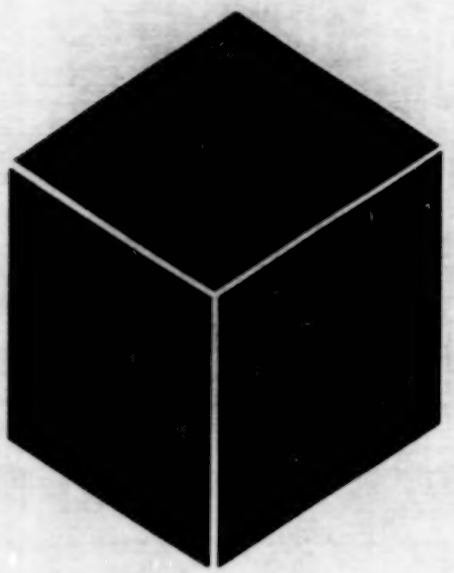

Materials

Hardware, Techniques, and Processes

31 $LaNi_{5-x}Sn_x$ Electrodes for Ni/MH Electrochemical Cells
32 Trading Risk Versus Cost of a Composite-Material Structure
33 $LaNi_{5-x}Ge_x$ Electrodes for Ni/MH Electrochemical Cells
34 Improved Bond-Coat Layers for Thermal-Barrier Coatings

BLANK PAGE

$LaNi_{5-x}Sn_x$ Electrodes for Ni/MH Electrochemical Cells

Capacities and cycle lives are increased.

NASA's Jet Propulsion Laboratory, Pasadena, California

Experiments have shown that improved hydride-forming negative electrodes for rechargeable nickel/metal hydride (Ni/MH) electrochemical cells can be made by substituting Sn for some of the Ni in $LaNi_5$. Since the year 1988, it has been known that partial substitution of Sn for some of the Ni in $LaNi_5$ slows the deterioration of reversible hydrogen-storage capacity and lowers the operating pressure for gas-phase cycling. However, prior to these experiments, the effects of the partial substitution on charge/discharge capacities on Ni/MH cells and on retention of their charge/discharge capacities during electrochemical reactions was not known.

Cyclic lifetime is an important issue in the technology of Ni/MH cells. Hydride-forming electrodes made of $LaNi_5$ undergo severe deterioration of charge/discharge capacities during charge/discharge cycling and thus have short cycle lives. It has been known since 1984 that the deterioration can be slowed by substituting small amounts of other elements for both La and Ni. Unfortunately, early attempts to prolong cycle lives in this way produced undesired side effects in the form of decreases in hydrogen-absorption capacities, slow kinetics, and prolongation of activation intervals (intervals of initial charge/discharge cycling needed to achieve full capacities).

The experiments showed that the electrochemical (charge/discharge) capacity of $LaNi_{5-x}Sn_x$ increases significantly with x up to about 0.25 (see Figure 1). The maximum discharge capacity observed in the experiments was slightly more than 300 mA·h/g — an impressive value for an alloy of this type and greater than the capacities (250 to 275 mA·h/g) of some of the misch-metal-based hydride-forming alloys that are being processed for electrodes in Japan and China. The substitution of Sn for some of the Ni results in low plateau pressures, with consequent low operating pressures and low self-discharge in alkaline rechargeable batteries.

The performances of $LaNi_{5-x}Sn_x$ alloys during charge/discharge cycling were evaluated in 250 mA·h, negative limited, prismatic laboratory cells (see Figure 2). The cells were designed in the MH-limited configuration to gain understanding of the life-limiting mechanisms of MH electrodes and to carry out a comparative evaluation of their cyclic lifetimes. Initial

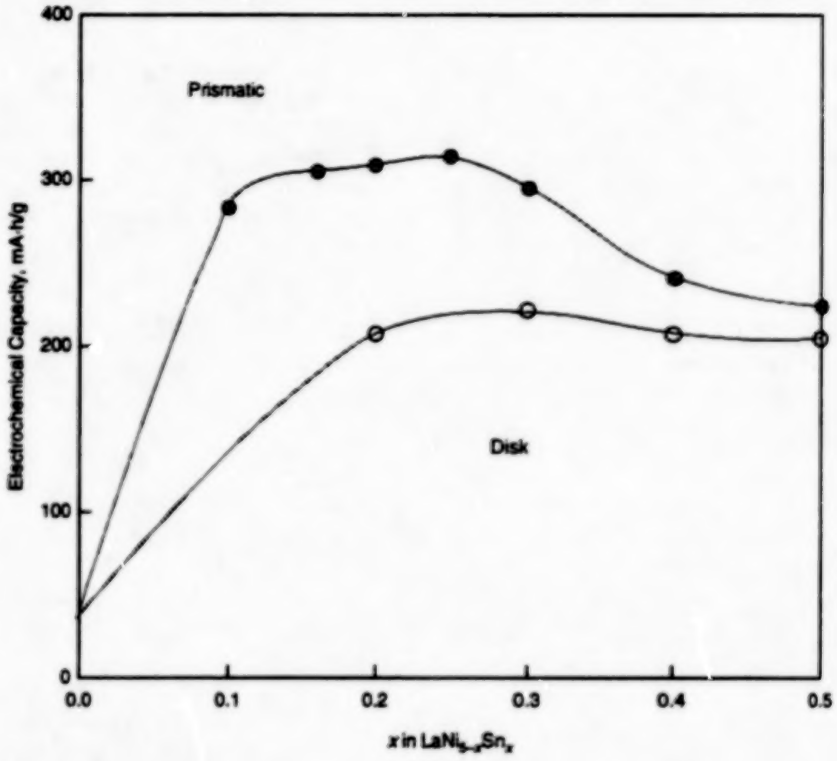

Figure 1. Electrochemical Capacities were measured on prismatic and disk specimens of $LaNi_{5-x}Sn_x$ with Sn concentrations ranging from 0 to 0.5.

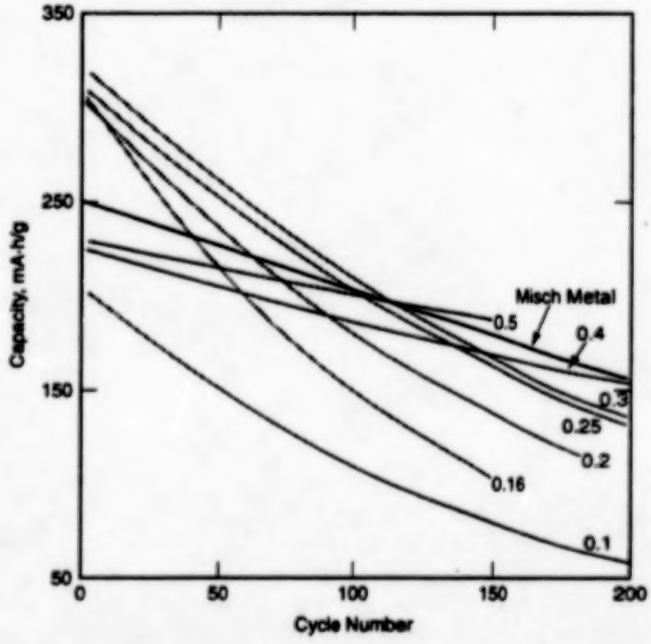

Figure 2. Capacities Retained After Charge/Discharge Cycling were measured on prismatic specimens of $LaNi_{5-x}Sn_x$ and on specimens of misch-metal-based hydride-forming alloys. The numbers alongside the curves denote the values of x in the $LaNi_{5-x}Sn_x$ alloys.

capacities were found to increase with x up to about 0.3 and then decrease with x beyond 0.3. After 100 full-capacity charge/discharge cycles, specimens with $x = 0.25$ and $x = 0.3$ exhibited capacities in excess of 200 mA·h/g — comparable to those of the best misch-metal-based alloys previously evaluated under identical conditions.

The capacities retained after 200 charge/discharge cycles were found to increase with x. Long activation intervals (30 charge/discharge cycles) were found to be necessary to achieve full capacities in the specimens with $x \geq 0.4$, but this is a relatively minor disadvantage in that after extensive charge/discharge cycling, these specimens emerged as the ones that retained the greatest capacities. These alloys with highest concentrations of Sn look promising for use at high temperatures, where the plateau pressures of other alloys are too high.

This work was done by Ratnakumar Bugga, Subbarao Surampudi, Brent Fultz, Charles K. Witham, Robert C. Bowman, Jr., and Adrian Hightower of Caltech for **NASA's Jet Propulsion Laboratory**. *Further information is contained in a TSP [see page 1].*

In accordance with Public Law 96-517, the contractor has elected to retain title to this invention. Inquiries concerning rights for its commercial use should be addressed to

Technology Reporting Office
JPL
Mail Stop 122-116
4800 Oak Grove Drive
Pasadena, CA 91109
(818) 354-2240

Refer to NPO-19805, volume and number of this NASA Tech Briefs *issue, and the page number.*

Trading Risk Versus Cost of a Composite-Material Structure

Tradeoffs are performed by use of a probabilistic method.

Lewis Research Center, Cleveland, Ohio

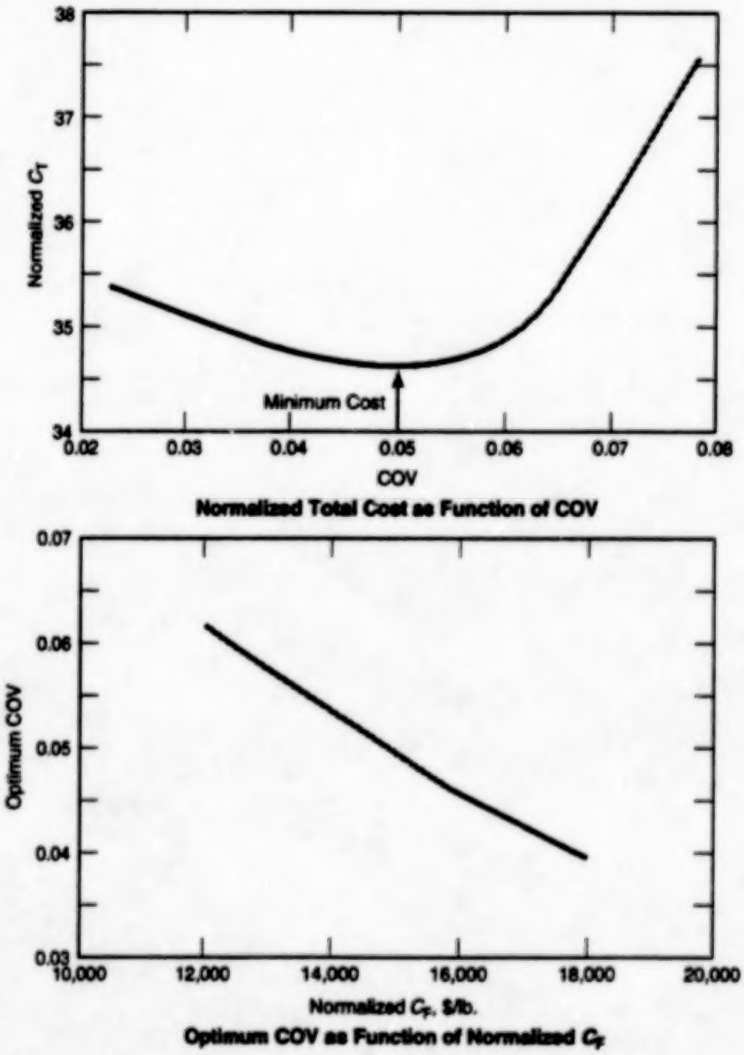

The Normalized Total Reliability-Based Cost (normalized C_T) in a test case was computed as a function of the COV for a normalized failure cost (normalized C_F) of $15,000/lb. The optimum value of the COV (the value for which the normalized C_T reached a minimum) was computed as a function of the normalized C_F.

A probabilistic method has been developed for use in designing a composite-material structure to achieve a balance between maximum reliability and minimum cost. This method accounts for all naturally occurring uncertainties in properties of constituent materials, fabrication variables, geometry, and loading conditions. Heretofore, it has been common practice to use safety factors (also called "knockdown factors") to reduce design loads on composite structures in the face of uncertainties. Safety factors often dictate designs of structures substantially heavier than they would otherwise be, but provide no quantifiable measures of reliability. The present method involves a quantitative approach to reliability; the equations of the method are formulated to yield a design that is optimum in the sense that it minimizes a reliability-based cost.

The derivation of the equations includes the definition of a probabilistic sensitivity that quantifies the change in reliability relative to a change in each random variable (design parameter). The probability of failure for a given performance is given by

$$P_f = \Phi(-\beta), \qquad (1)$$

where β is a reliability index and Φ is the cumulative distribution function of a normally distributed random variable. The probabilistic sensitivity factor for the ith random variable X_i is defined by

$$SF_i = \frac{\partial \beta}{\partial X_i} = \frac{u_i^*}{\beta} \qquad (2)$$

where u_i^* is the most probable failure point of a limit-state function in a unit normal probability space. The sensitivity

of the reliability index to the mean m_i of the normally distributed random variable X_i with standard deviation σ_i is given by

$$\frac{\partial \beta}{\partial m_i} = -\frac{SF_i}{\sigma_i} \qquad (3)$$

Similarly, the sensitivity of the reliability parameter to the standard deviation is given by

$$\frac{\partial \beta}{\partial \sigma_i} = -\frac{SF_i u_i^*}{\sigma_i} = -\frac{\left(u_i^*\right)^2}{\beta \sigma_i} \qquad (4)$$

The reliability-based total cost function, C_T, is the criterion that enables one to achieve the balance between reliability and cost. This function is given by

$$C_T = C_I + P_f C_F, \qquad (5)$$

where C_I is the cost of manufacture and C_F is the cost incurred in event of failure of the structure. The cost of manufacture can be expressed as

$$C_I = \sum_{j=1}^{N} C_j\left(p_j\right) + C_0 \qquad (6)$$

where p_j is a distribution parameter (which can be either m_j or σ_j), $C_j(p_j)$ is the manufacturing cost associated with the jth distribution parameter, and C_0 is a constant cost. The total cost can be minimized when

$$\frac{\partial C_T}{\partial p_j} = 0 \qquad (7)$$

for all j from 1 to N.

Then after substitution of terms from equations 1,5, and 6 and use of the chain rule for derivatives, equation 7 becomes

$$\frac{\partial C_j\left(p_j\right)}{\partial p_j} + C_F \frac{\partial \Phi\left(-\beta\right)}{\partial \beta} \frac{\partial \beta}{\partial p_j} = 0 \qquad (8)$$

for all j from 1 to N.

For a normally distributed random variable, $\partial\beta/\partial p_j$ can be calculated by equations 3 and 4. Equation 8 represents a system of N nonlinear equations that, if solved, yield a design with an optimum tradeoff between reliability and cost.

This method can be considered a special case of method for comprehensive probabilistic assessment of composite structures. The comprehensive method is implemented in the Integrated Probabilistic Assessment of Composite Structures (IPACS) computer code. [The comprehensive method was described from a slightly different perspective, with emphasis on computation of structural responses and fatigue lives, in "Probabilistic Analysis of Composite-Material Structures" (LEW-16092), *NASA Tech Briefs*, Vol. 21, No. 2 (February 1997), page 58.]

The method was demonstrated in test case in which the objective was to minimize the reliability-based cost of a lower side panel of a composite (graphite-fiber/epoxy-matrix) fuselage structure, using, as a design parameter, the coefficient of variation (COV) of the modulus of longitudinal elasticity of the graphite fibers. For the case studied, the minimum normalized total cost for a normalized failure cost of $15,000/lb ($33,000/kg) was found to occur at COV = 0.05. The optimum COV as a function of the normalized failure cost was also computed (see figure).

This work was done by Christos C. Chamis of **Lewis Research Center** *and Michael C. Shiao and Surendra N. Singhal of NYMA, Inc. Further information is contained in a TSP [see page 1].*

Inquiries concerning rights for the commercial use of this invention should be addressed to NASA Lewis Research Center, Commercial Technology Office, Attn: Tech Brief Patent Status, Mail Stop 7–3, 21000 Brookpark Road, Cleveland, Ohio 44135. Refer to LEW-16580.

$LaNi_{5-x}Ge_x$ Electrodes for Ni/MH Electrochemical Cells

Equilibrium pressures are decreased while capacities and cycle lives are increased.

NASA's Jet Propulsion Laboratory, Pasadena, California

Experiments have shown that improved hydride-forming negative electrodes for rechargeable nickel/metal hydride (Ni/MH) electrochemical cells can be made by substituting Ge for some of the Ni in $LaNi_5$. A similar discovery regarding the substitution of Sn for some of the Ni was reported in "$LaNi_{5-x}Sn_x$ Electrodes for Ni/MH Electrochemical Cells" (NPO-19805) page 31.

Hydride-forming electrodes made of $LaNi_5$ rapidly lose reversible hydrogen-storage capacities during charge/discharge cycling and thus have short cycle lives. It has been known for some years that the loss of reversible hydrogen-storage capacity can be slowed by substituting small amounts of other elements for both La and Ni. However, early attempts to prolong cycle lives through substitutions of elements other than Sn or Ge resulted in undesired side effects in the form of large decreases in hydrogen-absorption capacities, prolongation of activation cycles (cycles of initial charge/discharge cycling needed to achieve full capacities), or slow kinetics.

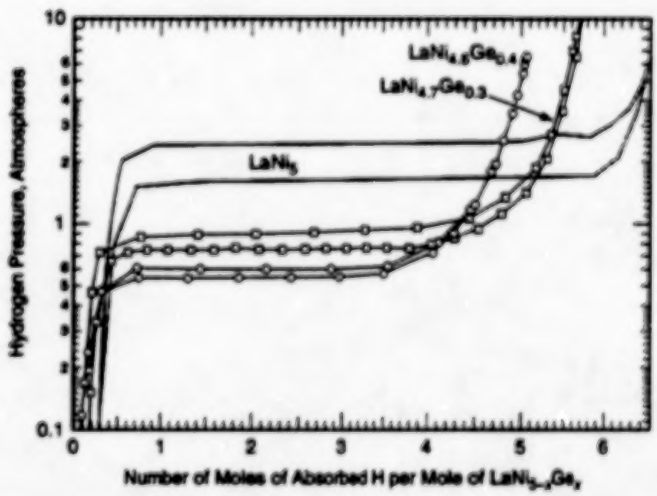

Figure 1. The Equilibrium Plateau Pressure for $LaNi_{5-x}Ge_x$ ($x > 0$) is less than 1 atmosphere — essential for preventing self-discharge in cells that must operate at atmospheric pressure.

Specimens of $LaNi_{5-x}Ge_x$ ($0.1 \leq x \leq 0.5$) for use in the experiments were made by induction melting in an argon atmosphere and annealed in vacuum at a temperature of 950 °C for 72 hours. In one of several experiments, gas-phase hydrogen-absorp-

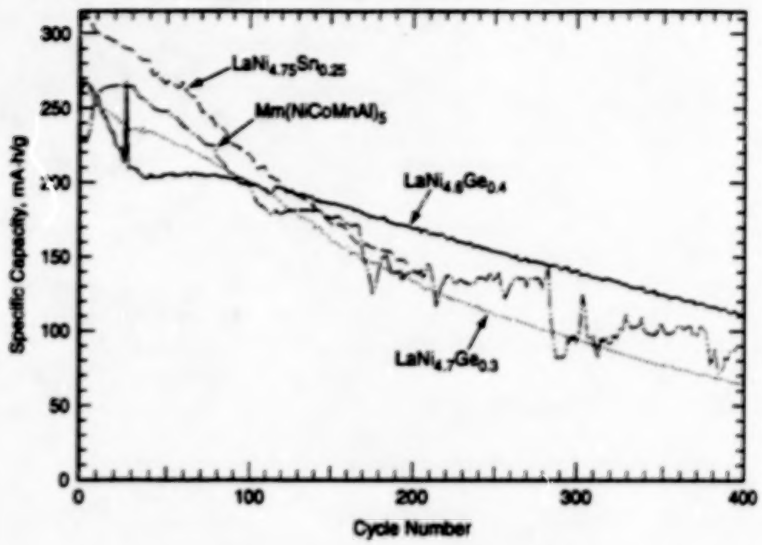

Figure 2. The Specific Charge Capacity retained after many charge/discharge cycles is greater for at least one of the Ge-substituted alloys than it is for the Sn-substituted alloy. The performance of a misch-metal-based alloy is also shown for comparison.

tion capacities of specimens with $x = 0, 0.3$, and 0.4 were measured at a temperature of 23 °C. The data from these measurements (see Figure 1) show that the gas-phase hydrogen-absorption capacities of the Ge-substituted alloys are marginally lower (a small disadvantage) than those of the binary alloy $LaNi_5$. However, the data also show a significant advantage for Ge substitution in that the equilibrium plateau pressure of the Ge-substituted alloys is less than 1 atm (< 0.1 MPa) — less than half the equilibrium plateau pressure of $LaNi_5$.

In another experiment, electrochemical capacities of prismatic $LaNi_{4.6}Ge_{0.4}$ and $LaNi_{4.7}Ge_{0.3}$ electrodes were measured in charge/discharge cycles in a negative-limited glass cell with NiOOH counter electrodes and an Hg/HgO reference electrode. For comparison, some measurements were performed on an Sn-substituted electrode with optimal composition of $LaNi_{4.75}Sn_{0.25}$, and on an electrode of composition $Mm(NiCoMnAl)_5$ (where "Mm" denotes misch metal). The data from this experiment (see Figure 2) show that all the alloys exhibit rapid loss of capacity during the first 10 to 20 cycles, but thereafter, the loss of capacity slows. The data also suggest that in the long term, the Ge-substituted alloys retain more capacity than does the optimal Sn-substituted alloy.

Another experiment focused on electrochemical kinetics for absorption and desorption of hydrogen. As quantified in terms of exchange-current densities, the kinetics of $LaNi_{4.6}Ge_{0.4}$ and $LaNi_{4.7}Ge_{0.3}$ were found to be improved over those of $LaNi_5$ — comparable to the kinetics of $LaNi_{4.8}Sn_{0.2}$.

In conclusion, the substitution of appropriate amounts of Ge for Ni in $LaNi_5$ results in alloys that are better suited for use in negative electrodes in rechargeable electrochemical cells. When developed further, these cells can be expected to exhibit high specific energy and power densities, low internal pressures and self discharge, and long cycle lives.

This work was done by Ratnakumar Bugga, Charles K. Witham, Brent T. Fultz, Subbarao Surampudi, Robert C. Bowman, and Adrian Hightower of Caltech for **NASA's Jet Propulsion Laboratory**. *Further information is contained in a TSP [see page 1].*

In accordance with Public Law 96-517, the contractor has elected to retain title to this invention. Inquiries concerning rights for its commercial use should be addressed to

Technology Reporting Office
JPL
Mail Stop 122-116
4800 Oak Grove Drive
Pasadena, CA 91109
(818) 354-2240

Refer to NPO-19962, volume and number of this NASA Tech Briefs *issue, and the page number.*

Improved Bond-Coat Layers for Thermal-Barrier Coatings

Compositions and processes are chosen to tailor microstructures and coefficients of thermal expansion.

Lewis Research Center, Cleveland, Ohio

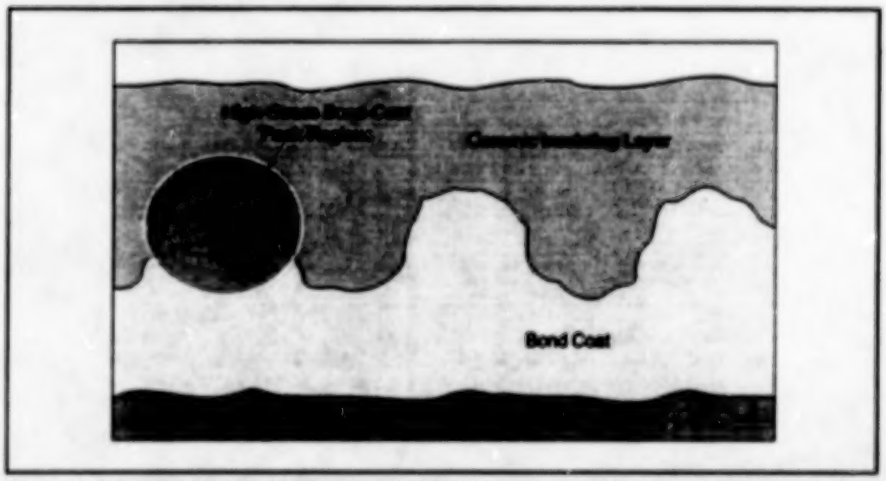

Figure 1. Schematic of a Typical Two-Layer TBC shows the area of high stress in the peak region.

Current production thermal-barrier coatings (TBCs) have been shown to be capable of reducing the average temperatures of metallic components by 50 to 80 °C and hot-spot temperature by up to 140 °C. This substantial temperature reduction has been used to extend the life of metallic components in aircraft turbines. However, for critical applications aimed at improving engine performance where significantly higher temperatures are involved, higher-durability TBCs are required. An improved bond coat incorporating metallic and cermet layers has been demonstrated to increase the thermal-fatigue life of a plasma-sprayed thermal-barrier coating (TBC) by a factor of two or more. These TBCs

can be applied to components in gas turbines and in diesel engines.

A typical TBC comprises a single metallic bond-coat layer, 0.005 to 0.008 in. (about 0.13 to 0.020 mm) thick, coated with a single ceramic top-coat layer, 0.005 to 0.020 in. (about 0.13 to 0.50 mm) thick. The bond-coat layer is typically MCrAlX, where M signifies Ni, Co, or Fe and X signifies Y, Zr, Hf, Yb, or another reactive element. The ceramic top-coat layer is typically zirconia partially stabilized with 6 to 8 weight percent of yttria. The bond coat is typically processed by plasma spraying, while the top coat can be processed by either plasma spraying or electron-beam physical vapor deposition. For TBCs using a plasma-sprayed top coat, the bond coat is prepared with a rough surface to improve bonding.

In spite of the necessity of bond-coat roughness to enhance adhesion, the roughness also tends to intensify the stresses that occur at the interface between the ceramic and the bond coat. Recent work has shown that the high stresses are particularly significant in the vicinity of the peaks in the rough bond coat (see Figure 1). Detailed investigation has further shown that the stresses can be minimized by matching the thermal expansion of the peaks of the bond coat to the ceramic top coat.

Figure 2 illustrates a TBC design that addresses these problems through the use of a two- layer bond coat. The first layer of the bond coat is a typical MCrAlX, as described for a conventional TBC above. The second layer of the bond coat incorporates a fine dispersion of a particulate second phase in an MCrAlX matrix. The second phase is required to have a coefficient of thermal expansion as low as, or preferably lower than, the yttria stabilized zirconia ceramic layer, it must be stable up to the intended use temperature, chemically inert with respect to the MCrAlX matrix, and must be chemically compatible with the thermally grown alumina scale. Candidate second-phase materials include alumina, chromia, yttrium-aluminum garnet, nickel-aluminum spinel, yttria, mullite, and other oxides.

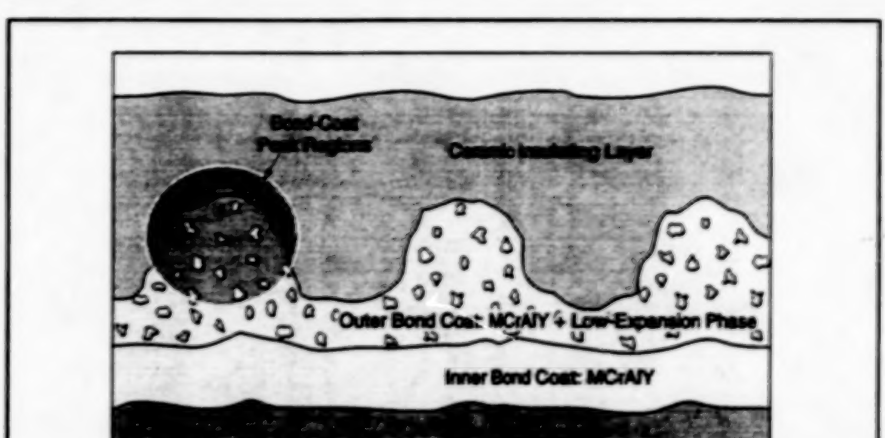

Figure 2. Fine Particles of a low-thermal-expansion phase are well dispersed in the matrix of the second bond-coat layer to reduce or eliminate the thermal expansion mismatch with the ceramic insulating layer.

Since the goal is to achieve expansion matching of the second-layer peaks to the yttria stabilized zirconia, the particulate second phase must have dimensions less than that of the peaks, typically less than 5 μm, and must be well dispersed in the MCrAlX matrix. The volume fraction of the particulate must be high enough to achieve substantial matching of the peak expansion to that of the ceramic layer. For the case of alumina additions to MCrAlX, an alumina volume fraction of 0.71 is required to achieve a near-zero thermal expansion mismatch. In practice, the thermal expansion of the second layer must be balanced against the other requirements for the layer, such as ductility and oxidation resistance.

Coatings to date have been plasma sprayed using starting powders produced by mechanical alloying. The mechanical-alloying process that has been developed has produced plasma-spray starting powders with up to 20 volume percent of a fine dispersion of submicron alumina particles. The ceramic layer life was doubled for TBCs, using a bond coat of only 5 volume percent alumina additions. This technologically important, and repeatable, increase in life could be used to push the TBCs to higher operating temperatures.

Higher volume percentages of alumina, up to 20 volume percent, were expected to provide even longer lives due to better expansion matching with the ceramic. While some samples did exhibit longer lives, these compositions also exhibited widely varying oxidation responses. The net result of the erratic oxidation response was a reduction in the average life for these coatings. Alternative thermal-spray processes, such as high-velocity oxy-fuel spraying (HVOF), have proven to produce more homogeneous particle distributions and hold the promise of even higher gains in TBC life. The HVOF coatings are currently being tested.

This work was done by William J. Brindley and Robert A. Miller of **Lewis Research Center** *and Beverly J. M. Aikin of Case Western Reserve University. Further information is contained in a TSP [see page 1].*

Inquiries concerning rights for the commercial use of this invention should be addressed to NASA Lewis Research Center, Commercial Technology Office, Attn: Tech Brief Patent Status, Mail Stop 7–3, 21000 Brookpark Road, Cleveland, Ohio 44135. Refer to LEW-16390.

BLANK PAGE

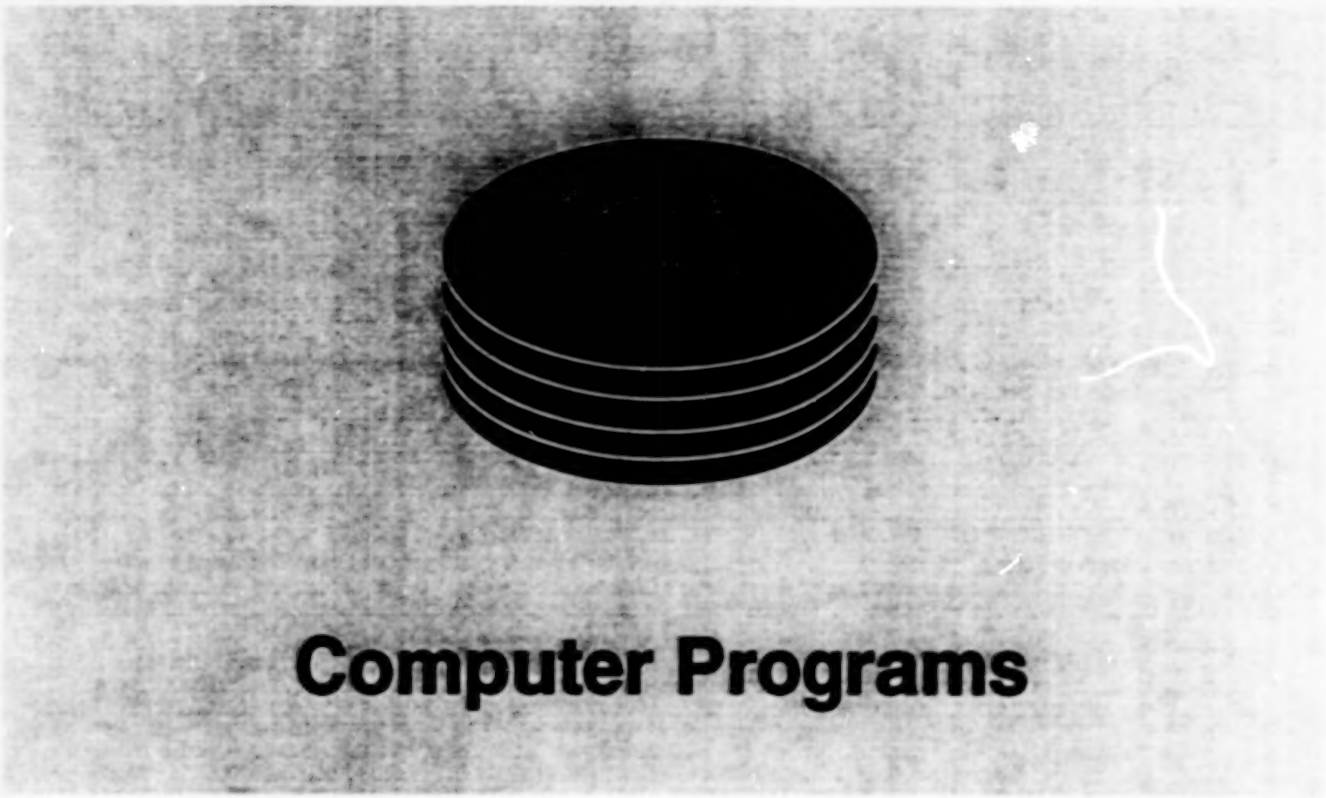

Computer Programs

Mechanics

39 Updated Program for Computing Stresses in Spur Gears

BLANK PAGE

Computer Programs

These programs may be obtained from COSMIC. Please contact

COSMIC®
Computer Services Annex
University of Georgia
Athens, GA 30602
Telephone No. (404) 542-3265.

Mechanics

Updated Program for Computing Stresses in Spur Gears

This software can be used for parametric studies of static and dynamic effects.

DANST-PC is version 3.01 of a computer program for analysis of the statics and dynamics of spur-gear systems. ["DANST" signifies "Dynamic Analysis of Spur Gear Transmissions." A previous version was described in "Computing Stresses in Spur Gears," *NASA Tech Briefs*, Vol. 19, No. 12 (December 1995), page 73.] The program can be used for parametric studies to predict the static transmission error, dynamic load, tooth-bending stress, and other properties of a pair of external spur gears as they are influenced by operating speed, torque, stiffness, damping, inertia, and tooth profile. DANST performs geometric modeling and dynamic analysis for low- or high-contact-ratio spur gears. It can simulate gear systems with contact ratios ranging from one to three.

DANST is based on a four-degree-of-freedom, lumped-mass model of a gear transmission. The model includes driving and driven gears, connecting shafts, motor, and load. The equations of motion were derived from basic gear geometry and elementary vibration principles. The dynamic solution is found by integrating the equations of motion. The user is provided with many options, including (1) materials, basic gear geometries, and operating conditions; (2) various combinations of tooth profiles (including standard forms of tip relief or user-digitized profile modifications); (3) static or dynamic analysis; and (4) various printed and plotted outputs.

DANST is written in FORTRAN 77 for i386 and above IBM-PC-compatible computers running the MS-DOS, Windows95, or Windows NT operating system. A math coprocessor and VGA display are required. The source code and executable code are provided. DANST-PC has been successfully implemented on an i486DX computer running Windows95. To recompile the source code, one needs the plotting software package PLOT88 from Plotworks Software. The standard distribution medium for DANST-PC is one 3.5-in. (8.89-cm), 1.44MB diskette in MS-DOS format. DANST-PC was released to COSMIC in 1997.

This program was written by Fred B. Oswald of **Lewis Research Center**, *Hsiang H. Lin of the University of Memphis, and Irebert R. Delgado of the U.S. Army. Further information is contained in a TSP* *[see page 1]*.
LEW-16575

BLANK PAGE

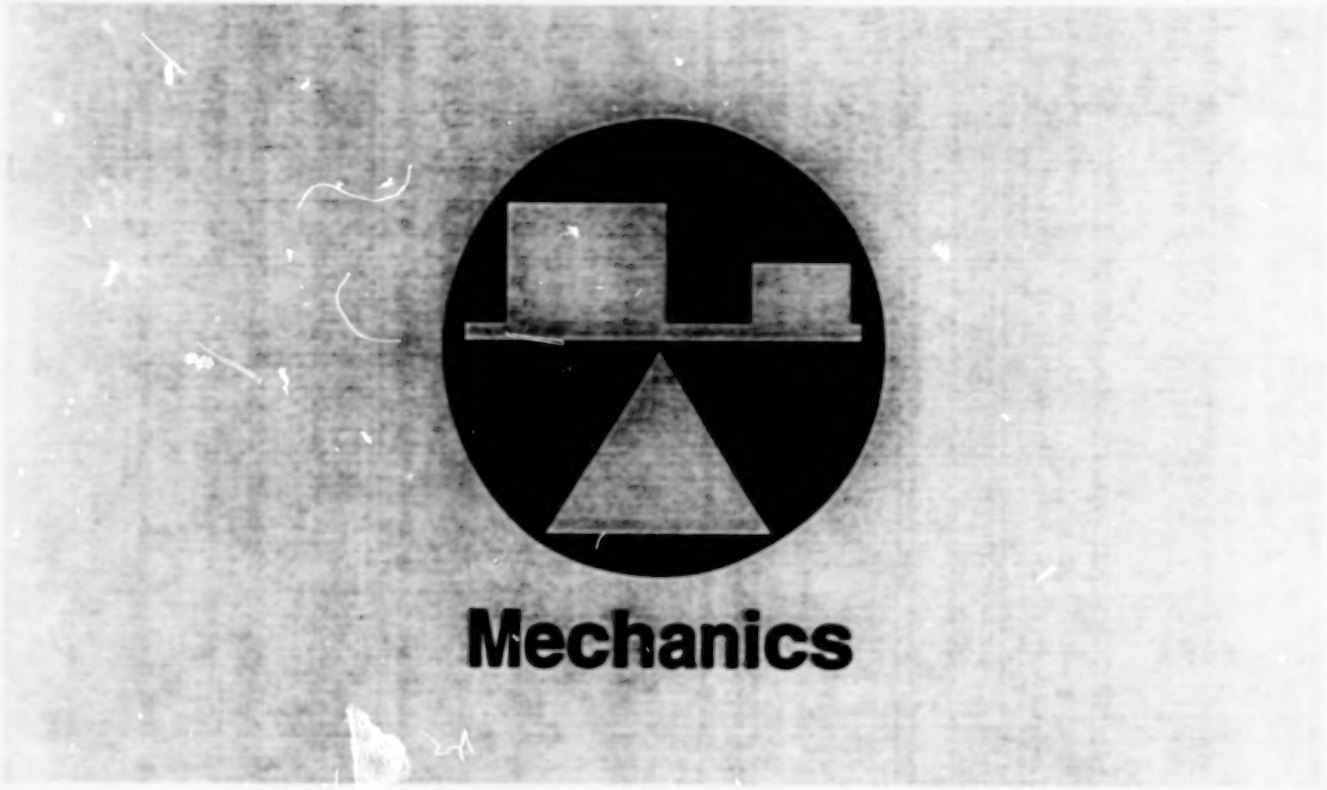

Hardware, Techniques, and Processes

43 Subliming Solid Microthrusters
43 Trefoil Rotary Flexure

BLANK PAGE

Subliming Solid Microthrusters

Devices using solid propellants would eliminate waste and leakage common with gaseous propellants.

NASA's Jet Propulsion Laboratory, Pasadena, California

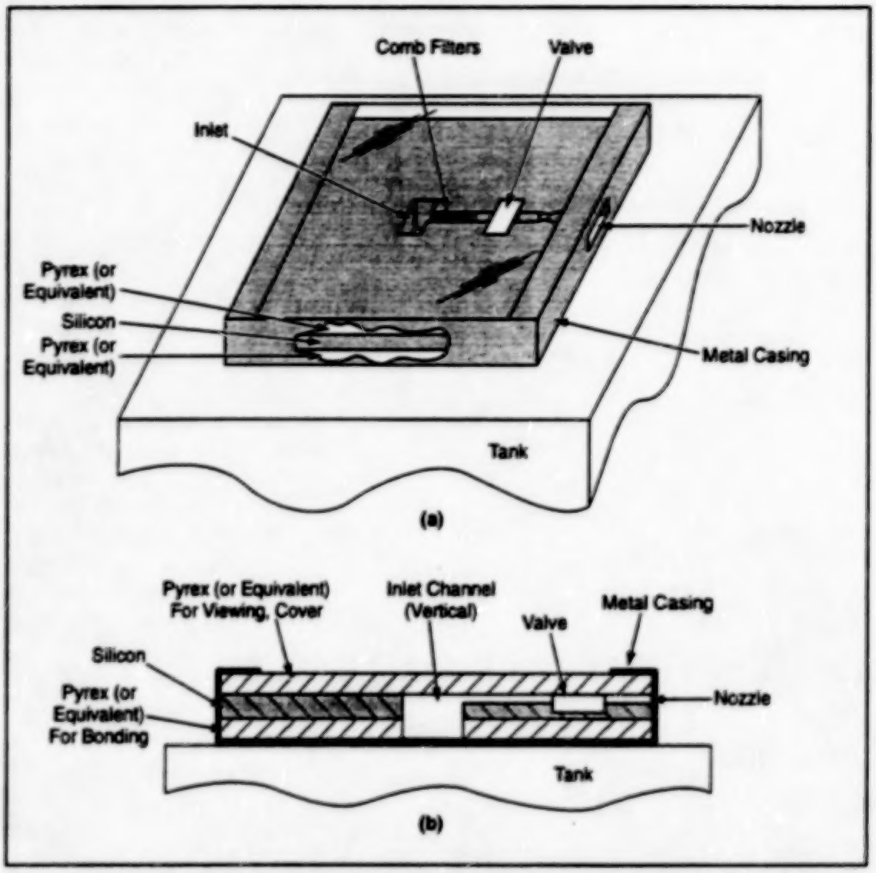

Figure 1. The Concept of the Subliming Solid Microthruster is illustrated in oblique view (a) and side view (b).

Devices are proposed that would sublime solid propellants to generate small thrusts for maneuvering spacecraft with masses of no more than 15 kg. With solids rather than gases in propellant tanks, there would be no leakage and thus no waste of limited quantities of propellants. There would also be none of the bulk, weight, and cost of plumbing like that needed for handling liquid or gaseous propellants if the propellant tank would be integrated with the subliming solid thruster.

The propellant in a subliming thruster would be contained in an aluminum tank (see Figure 1) with an outlet connected to the subliming solid microthruster chip. This chip, micromachined from silicon, contains a nozzle and an integrated filter. Ultimately, a thruster valve will also be integrated into this chip. A wire electric heater could be wrapped around the tank, or else a film electric heater could be deposited on the tank. The propellant material (e.g., ammonium hydrosulfide) would be sublimed on command by activating the heater.

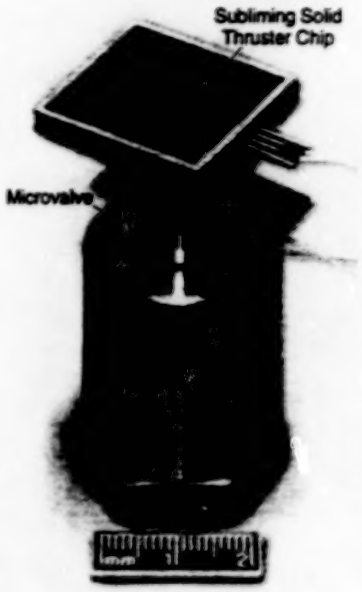

Figure 2. Microthruster Model shows the level of miniaturization that can replace bulkier units.

Opening a valve placed into a flowpath between the nozzle and tank (see Figure 2) will allow the vapor to flow to whichever nozzle faced in the direction opposite the required direction of thrust. The wall of the tank could be as thin as 0.020 in. (0.5 mm) because the vapor pressure that it would have to withstand would be very small; thus, the tank could be very light in weight.

This work was done by Juergen Mueller, Lilac Muller, and Thomas George of Caltech for **NASA's Jet Propulsion Laboratory**. *Further information is contained in a TSP [see page 1].*

NPO-19926

Trefoil Rotary Flexure

Tri-lobed inner support enables low rotational stiffness while providing rigidity for high radial and axial stiffnesses.

NASA's Jet Propulsion Laboratory, Pasadena, California

The figure illustrates a device that flexes to allow rotation about a single axis through a total range of ±12°. This device was designed to offer the following advantages over commercial flexural pivots:

- Greater ratios of radial to rotational and axial to rotational stiffness for a given load capability;
- Higher load capabilities for a given rotational stiffness;
- No shift in the center of rotation assuming flexures are uniform in thickness;
- Theoretical unlimited fatigue life at ±10° excursion;
- Monolithic construction for higher reliability and greater likelihood of attaining the theoretical fatigue life; and
- No global buckling modes.

The device is called a "trefoil rotary flexure" because its flexible members are three radial, equally spaced thin plates that extend from an outer cylinder to the inner tri-lobed support. The distance from the inner terminus of the flexures to the rota-

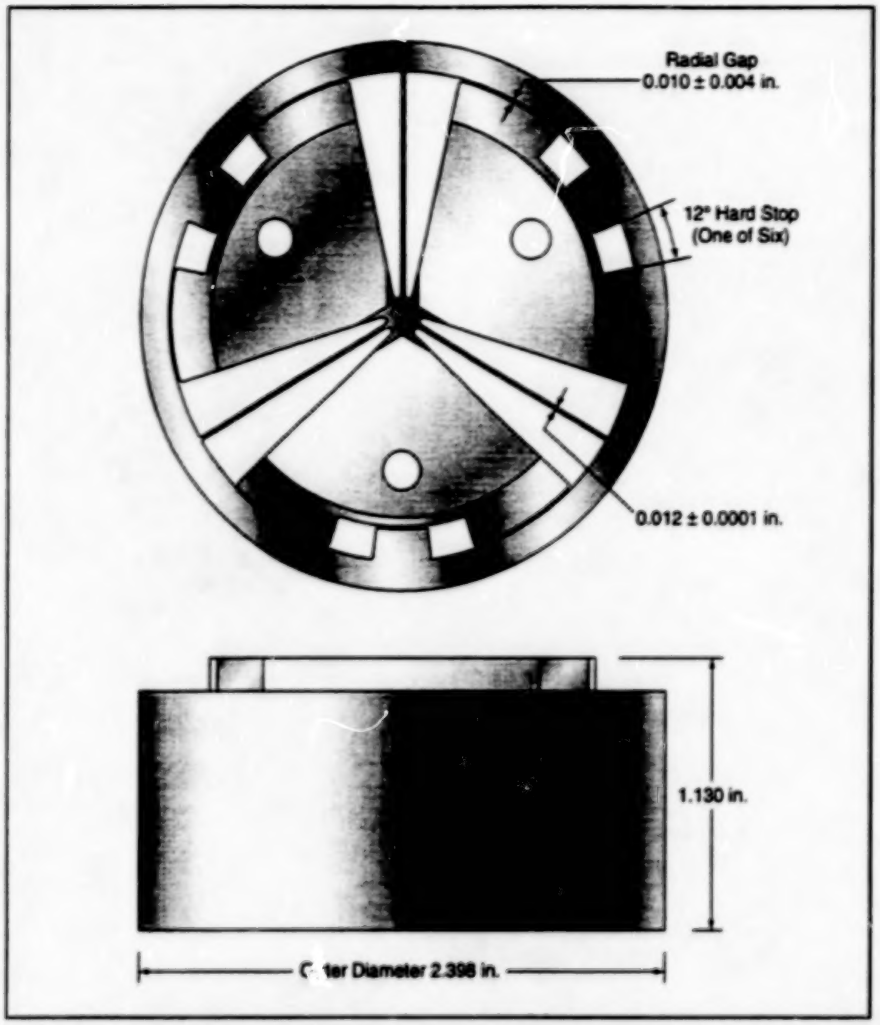

This **Trefoil Rotary Flexure** is a monolithic device, machined from a solid metal rod. It is designed for high radial and axial stiffness, low rotational stiffness, and long fatigue life.

tional axis is made as small as possible to minimize rotational stiffness. The three lobes of the inner support are joined at the rotation axis to provide an extremely rigid attachment for the flexure elements, allowing high radial and axial stiffnesses. The tri-lobed support rotates relative to the outer cylinder on the flexures to create the flexural pivot motion. The total rotational range of ±12° is defined by hard stops in the lobes and the outer cylinder.

The lobes, fins, and outer cylinder are integral parts of the monolithic device, which was fabricated by electrical-discharge machining of a solid metal rod. To reduce concentrations of stresses and thereby ensure long fatigue life, generous fillet radii were incorporated at the inner and outer ends of the fins.

This work was done by Robert J. Calvet of Caltech for **NASA's Jet Propulsion Laboratory**. *Further information is contained in a TSP [see page 1].*

In accordance with Public Law 96-517, the contractor has elected to retain title to this invention. Inquiries concerning rights for its commercial use should be addressed to

Technology Reporting Office
JPL
Mail Stop 122-116
4800 Oak Grove Drive
Pasadena, CA 91109
(818) 354-2240

Refer to NPO-20228, volume and number of this NASA Tech Briefs *issue, and the page number.*

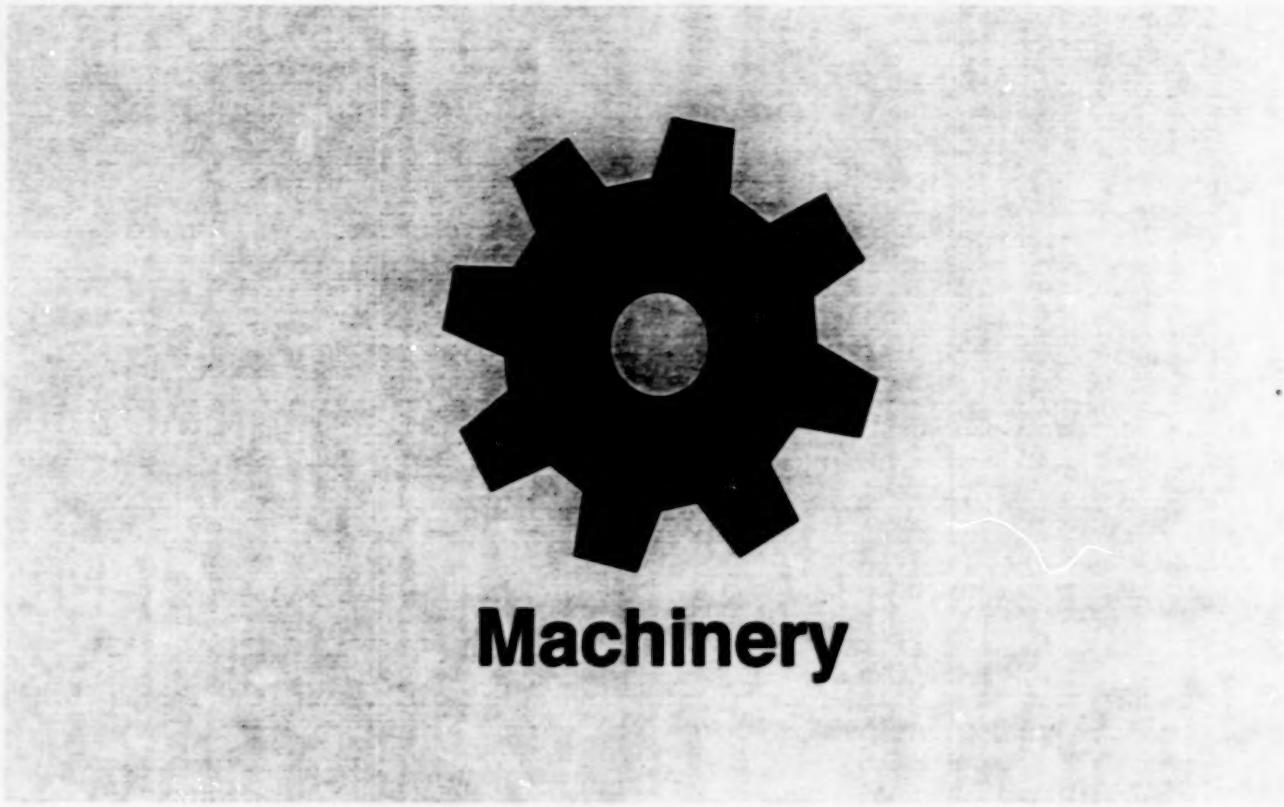

Machinery

Hardware, Techniques, and Processes

47 Snakelike Robots Would Maneuver in Tight Spaces
48 Wavy Blades for Secondary Centrifugal Blood-Pump Impeller
49 Doped ZnTe: a Developmental Photorefractive Material
50 Jewellike Bearings for Blood Pumps

BLANK PAGE

Snakelike Robots Would Maneuver in Tight Spaces

Potential applications include inspection, maintenance, and surgery.

NASA's Jet Propulsion Laboratory, Pasadena, California

Robots with multiple-link arms that could reach through narrow openings into hidden cavities are undergoing development. Called "multifunction dexterous boro-robots" (MDBRs), these robots would resemble snakes (see Figure 1), in both general appearance and in the slithering motion with which they would negotiate narrow passages. Robots like these could make it possible to inspect, maintain, and repair critical parts in the interiors of complex machines like aircraft engines, without having to take the machines apart and then putting them back together at great expense. Such robots could also prove useful as surgical endoscopic tools. In comparison with currently available borescopes and endoscopes, MDBRs would be more versatile, more controllable, and better able to maneuver around obstacles. The MDBRs would differ from the serpentine inspection robots reported previously in *NASA Tech Briefs* [see "Small, Lightweight Inspection Robot With 12 Degrees of Freedom" (NPO-19367) Vol. 20, No. 2 (February 1996), page 73 and "Control of a Serpentine Robot for Inspection Tasks" (NPO-19506) Vol. 20, No. 3 (March 1996), page 1b.]

Each link in an MDBR contains linear actuators that are part of a kinematic linkage for controlling the relative orientations of the adjacent links. The kinematic linkage (see Figure 2) includes a base plate at one end and an articulation plate at the other end. The base and articulation plates also serve as the articulation and base plates, respectively, of the preceding and following links. The base and articulation plates are connected by six struts with compensated universal joints at their ends.

Three of the struts are of fixed length and are crossed; three of the struts are the linear actuators and are not crossed. Together, the six struts and the base and articulation plates constitute a truss with a unique configuration and a high strength-to-weight ratio. The configuration of the truss (and thus the position and orientation of the articulation plate relative to the base plate) can be altered by commanding the linear actuators to change their lengths according to the kinematical requirements. The linear actuators could be of any of several types; miniature piezoelectric "inchworm" actuators are particularly suitable.

The individual actuator commands to obtain the overall desired pose and snake-like motion of the arm are generated by a computer that solves the equations for both the forward and the inverse kinematics of the links and of the whole arm. An MDBR is modular in the sense that in principle, any number of links [with the same or different diameter(s) and length(s)] can be added to extend its reach or increase its dexterity. A two-link prototype has been demonstrated. In a practical application, the benefits of increased dexterity and reach would have to be traded off against the increase in the amount of computation needed to solve the inverse kinematical equations for a greater number of links.

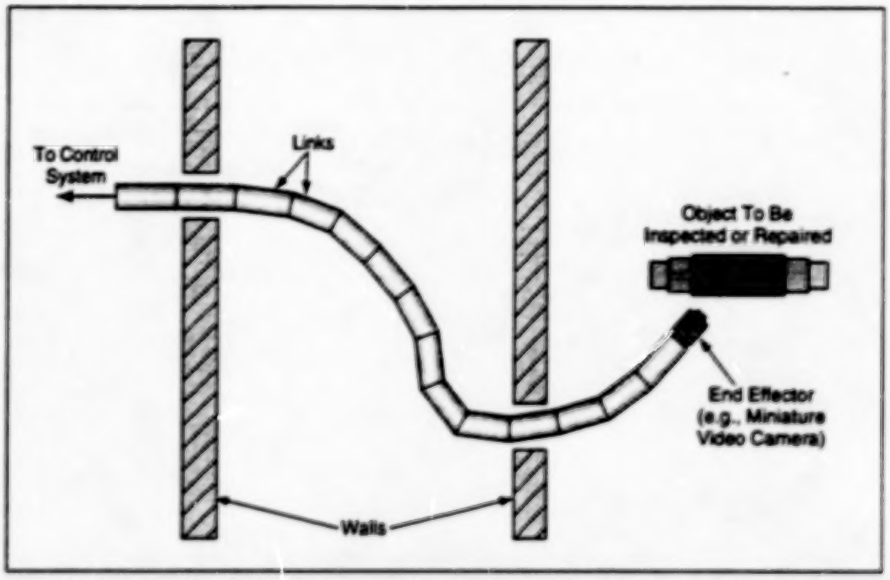

Figure 1. A Serpentine Robot Arm comprising many lightweight, rigid links could be maneuvered through narrow openings to reach objects that would otherwise be inaccessible. Each link could be made less than 1 cm in diameter and would typically be several centimeters long. The robot arm would be covered by a sheath of flexible material to protect the mechanisms in the links.

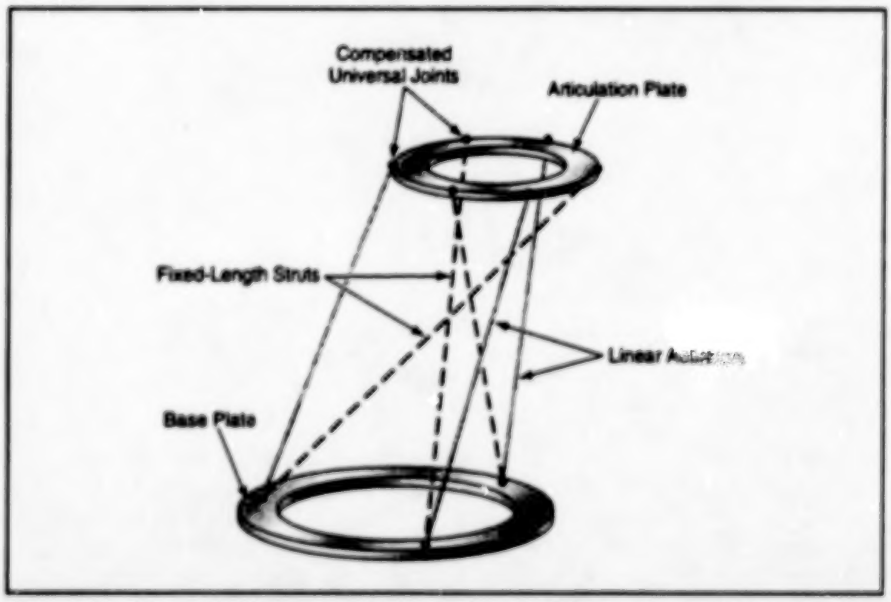

Figure 2. The Kinematic Linkage in each link provides control of the position and orientation of the articulation plate relative to the base plate. The base and articulation plates are shown here as circular disks, but they could just as well have triangular or any other suitable shape.

This work was done by Yoseph Bar-Cohen and Mohsen Shahinpoor of Caltech for **NASA's Jet Propulsion Laboratory**. *Further information is contained in a TSP [see page 1].*

In accordance with Public Law 96-517, the contractor has elected to retain title to this invention. Inquiries concerning rights for its commercial use should be addressed to

Technology Reporting Office
JPL
Mail Stop 122-116
4800 Oak Grove Drive
Pasadena, CA 91109

(818) 354-2240
Refer to NPO-20268, volume and number of this NASA Tech Briefs issue, and the page number.

Wavy Blades for Secondary Centrifugal Blood-Pump Impeller

The flow pattern would be modified to reduce the tendency toward clotting.

Lewis Research Center, Cleveland, Ohio

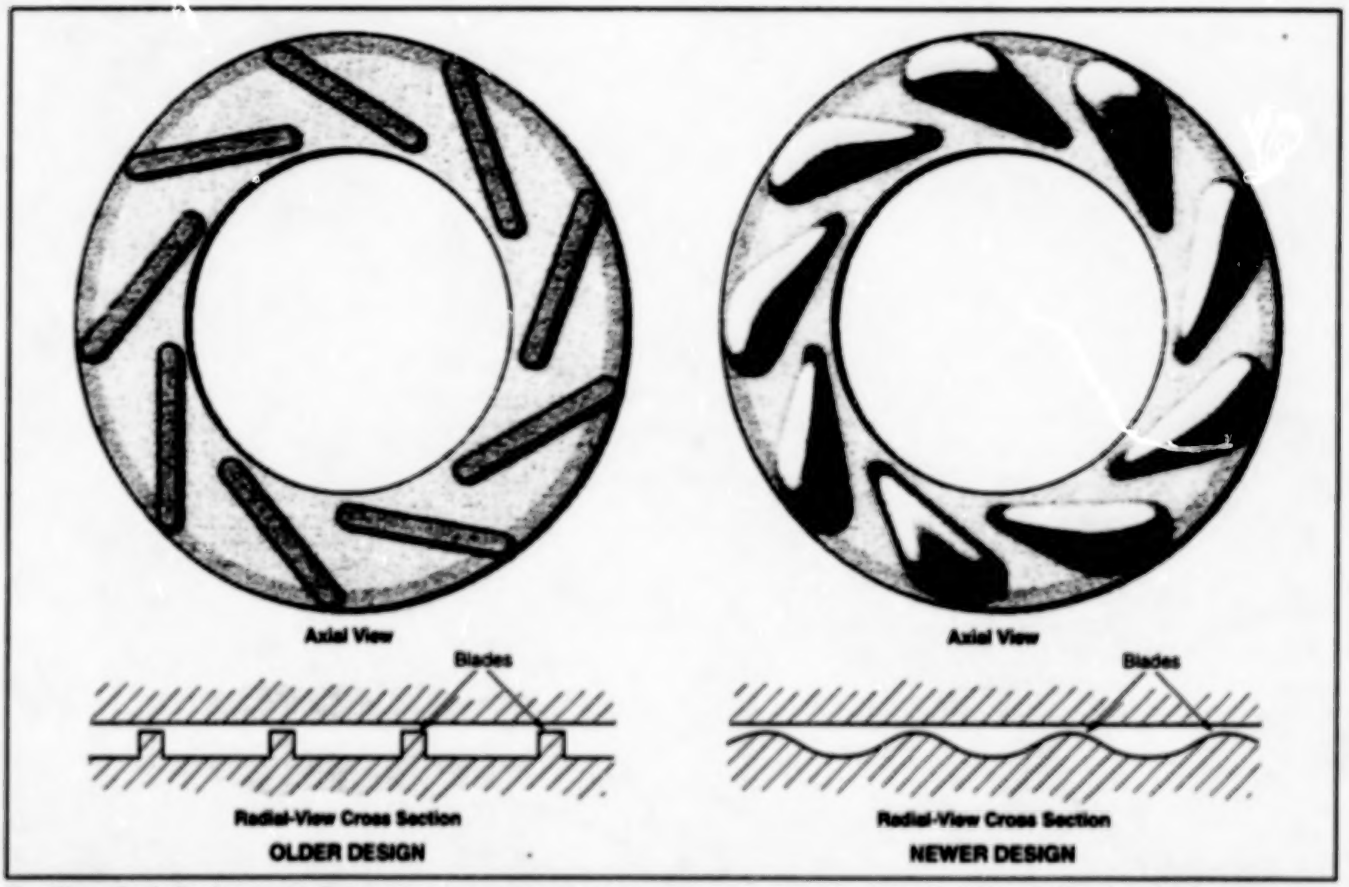

The Wavy-Blade Design would eliminate the square corner regions where recirculation tends to occur, and would reduce the flow cross section, thereby reducing residence time.

The rectangular-cross-section blades of a centrifugal secondary impeller in a ventricular-assist blood pump would be replaced with blades of wavy cross section, according to a proposal. As explained below, the resulting modification in the flow pattern would reduce the tendency toward clotting.

The function of the secondary impeller in a centrifugal-assist blood pump is to deliver a flow of ≤0.1 liter per minute through a fluid film bearing. The wavy-blade concept would be primarily advantageous at flow rates ≤0.1 liter per minute, but could also be applied, if necessary, to blood-pump impellers with nominal flow rates as large as 5 liters per minute, in cases in which blood would otherwise coagulate on blades, forming deposits that would eventually grow to block flow passages.

The figure illustrates the older and the proposed newer designs. In the older design, the square corner regions of the passages between the blades accommodate the formation of pockets of recirculation, which can cause coagulation and deposition of blood on the blades. Recirculation also gives rise to long residence times within the passages, thereby triggering the onset of coagulation within the blood and increasing the deposition on the blades.

The adoption of the proposed wavy (nearly sinusoidal) cross sections of the proposed impeller blades would effectively reduce the sizes of the corner regions, reducing the tendency for pockets of recirculation to form. The average thicknesses of the wavy blades would be greater than those of the rectangular blades; in other words, the cross-sectional areas of the passages between blades would be reduced. As a result, the residence time for a given flow rate would be reduced.

This work was done by Joseph P. Veres of **Lewis Research Center.** *Further information is contained in a TSP (see page 1).*

Inquiries concerning rights for the commercial use of this invention should be addressed to NASA Lewis Research Center, Commercial Technology Office, Attn: Tech Brief Patent Status, Mail Stop 7-3, 21000 Brookpark Road, Cleveland, Ohio 44135. Refer to LEW-16447.

Doped ZnTe: a Developmental Photorefractive Material

This material can be used in optical processing of information at wavelengths from 0.6 to 1.3 μm.

Lewis Research Center, Cleveland, Ohio

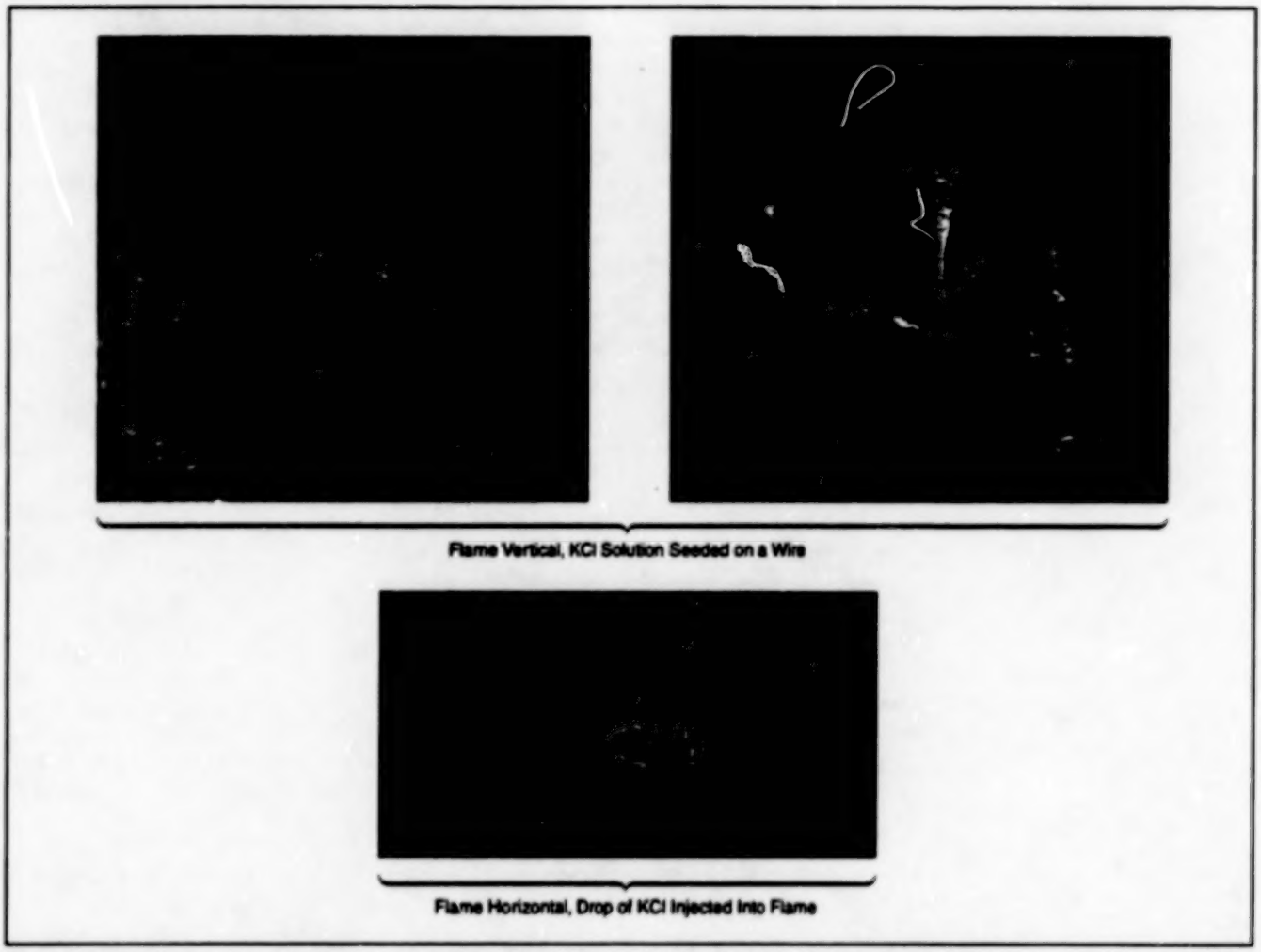

These Interferograms, generated by resonant holographic interferometric spectroscopy, illustrate the distribution of potassium seeded into three butane diffusion flames. Taking advantage of the rapid response of a photorefractive semiconductor like ZnTe:V:Mn, one can acquire such images at video frame rates.

Zinc telluride is a semiconductive material that has been found to become photorefractive when it is suitably doped with vanadium or with manganese and vanadium. The combination of photorefractivity and semiconductivity make this material attractive for use in a variety of applications, including optical power limiting (for shielding eyes or delicate sensors against intense illumination), holographic interferometry, providing reconfigurable optical interconnections for optical computing and optical communication, and correcting for optical distortions and combining laser powers via phase conjugation. In comparison with other important photorefractive materials based on III-V and II-VI binary compounds, ZnTe:V offers superior photorefractive performance at wavelengths from 0.6 to 1.3 μm.

Undoped or doped ZnTe can be grown by physical vapor transport in a closed ampoule. The source material lies at one end of the ampoule and is made to sublimate by heating that end to a suitable temperature. The resulting vapor is transported to the other, cooler end of the ampoule, where it condenses to form a boule of the material. Ideally, the boule thus formed should be a single crystal (as distinguished from a polycrystalline mass). For successful growth of a single crystal, it is necessary to adjust the thermal gradient and other conditions to make the rate of transport commensurate with the rate of integration of condensing molecules and atoms into the growing crystal.

In an effort to learn how to optimize conditions for single-crystal growth, the diffusive and convective effects of heat and mass transfer have been investigated both experimentally and theoretically. Topics addressed in these investigations have included effects of process parameters, effects of buoyancy-driven convection on transport properties, growth fluxes, and crystal-growth rates (deduced from growth fluxes, assuming fast kinetics at growth interfaces). The results of these investigations indicate that for a given gradient of temperature, the ratio between the partial pressures of Zn and Te at the source strongly affects the rate of transport. The rate of growth changes with both the temperature and the gradient of temperature between the source and the growing crystal.

Experiments have been performed to determine the optical absorption spectra, electrical resistivities, photorefractive prop-

erties, and microstructures of specimens of doped ZnTe. Among other things, it has been found that the yield of photorefractive crystals is very low when vanadium is the only dopant, but that one can increase the yield, the photorefractive gain, and the diffraction efficiency by doping with manganese in addition to vanadium.

An experiment was performed to investigate optical power limiting in ZnTe:V by the field-shielding effect, which is a nonlinear effect that occurs in the presence of an applied electric field and that results in partial darkening. For example, in one case, the transmission of a specimen at a wavelength of 0.83 μm was 20 percent at an incident radiant flux density of 6 mW/cm^2, but decreased to 1 percent when the flux density was increased to 1 W/cm^2.

Experiments were performed to investigate the utility of ZnTe:V:Mn for real-time resonant holographic interferometry. These experiments involved, variously, two- or four-wave mixing, using pulsed dye or continuous-wave He/Ne or diode lasers. Holographic image transfer and two-wavelength resonant holographic interferometry were demonstrated; in particular, a ZnTe:V:Mn crystal was used in a demonstration of resonant holographic interferometric spectroscopy, which is a technique for obtaining chemical-species-specific interferograms by recording two holograms simultaneously at two slightly different wavelengths near an absorption spectral peak of the species in question (see figure).

This work was done by Walter M.B. Duval of **Lewis Research Center**; *Sudhir B. Trivedi, G. V. Jagannathan, Xiaolu Wang, Jolanta I. Soos, and Robert D. Rosemeier of Brimrose Corp.; H. Zhou and Abdelfattah Zeblo of Rutgers University; and W. H. Steier and Mehrdad Ziari of the University of Southern California. Further information is contained in a TSP [see page 1].*

Inquiries concerning rights for the commercial use of this invention should be addressed to NASA Lewis Research Center, Commercial Technology Office, Attn: Tech Brief Patent Status, Mail Stop 7–3, 21000 Brookpark Road, Cleveland, Ohio 44135. Refer to LEW-16498.

Jewellike Bearings for Blood Pumps

Clots are reduced because blood is not forced through small clearances.

Lyndon B. Johnson Space Center, Houston, Texas

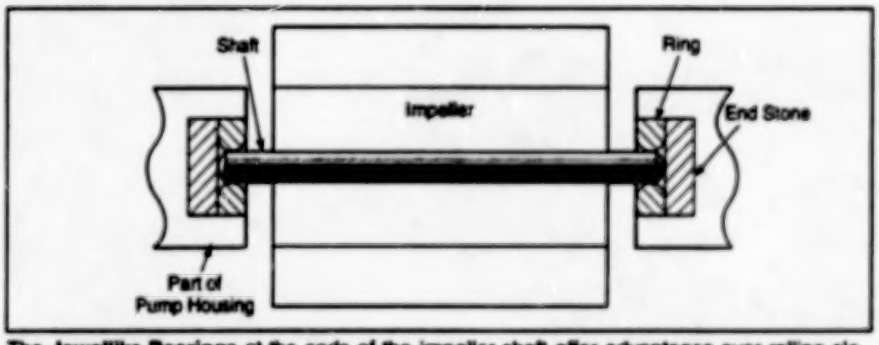

The Jewellike Bearings at the ends of the impeller shaft offer advantages over rolling-element, pivot, and journal bearings.

Jewellike bearings have been devised to enhance the performance and safety of small rotary pumps that are used to increase or sustain flows of blood in cardiac patients. A pump of this type includes a spinning impeller in an axial- or radial-flow configuration. The impeller shaft is supported at its ends by the jewellike bearings. Similar bearings could be used in other small pumps that are required to operate for long times without need for maintenance.

The jewellike bearings are designed to overcome the deficiencies of older rolling-element, pivot, and journal bearings. One of the chief deficiencies is susceptibility to pump seizure caused by the accumulation of coagulated blood in narrow flow passages and in voids within bearings. In the case of journal bearings, another notable deficiency is damage to red blood cells and generation of microclots in high-shear flows of blood through the narrow journal gaps.

In a pump, the jewellike bearings at both ends of the impeller shaft are identical. Each bearing (see figure) includes the end portion of the shaft, a ring, and an end stone. The rings support the shaft radially, while the end stones sustain thrust (axial) loads and limit axial movement of the shaft. The inner surface of the ring facing the shaft is rounded for line contact with the shaft, and the tips of the shaft are rounded for point contact with the end stones; these line- and point-contact features reduce bearing friction and thereby reduce the power needed to drive the pump.

The radial clearance between the shaft and ring is typically 0.0001 to 0.0002 in. (0.0025 to 0.005 mm). The shaft end play (axial clearance) is typically 0.005 to 0.010 in. (0.13 to 0.25 mm). The bearing components can be made of ceramics or hardened metals.

The jewellike bearings offer several advantages:

- Unlike rolling-element bearings in which shaft seals are used to keep blood from entering voids, these bearings can function without shaft seals. Any blood that enters the small void in either bearing coagulates quickly, but in so doing, it forms a smooth surface that conforms to the end of the shaft and thus does not interfere with the rotation of the shaft. Moreover, the diameter of the shaft can be made very small so that any increase in friction caused by the coagulated blood results in only a small increase in frictional torque.
- The configuration of the rounded inner ring surface and the mating cylindrical lateral shaft surface provides the precise clearance fit needed for precise rotation of the shaft, yet accommodates misalignment of the shaft.
- No axial-preload mechanism is needed because the pump is designed to operate with shaft end play.
- Because the bearing surfaces are in contact with each other, there is no need for the additional pump, reservoir, and/or complex plumbing that would be needed if the design relied on fluid pressure (as in some journal bearings) to carry the bearing loads.
- Blood trauma and potential clotting are reduced in that blood is not forced through narrow gaps.

This work was done by Greg S. Aber of **Johnson Space Center**. *Further information is contained in a TSP [see page 1].*

This invention is owned by NASA, and a patent application has been filed. Inquiries concerning nonexclusive or exclusive license for its commercial development should be addressed to the Patent Counsel, Johnson Space Center, (281) 483-0837. Refer to MSC-22721.

National Aeronautics and
Space Administration

END

10/13/98